NTNU
Norwegian University of
Science and Technology

A TEM Study of Weakly Overaged Precipitates in AA 6082

Olav Sulen

Abstract

New models for modeling the material properties for aluminium alloys that can take into consideration the geometry of the needle shaped precipitates, that can be found in 6xxx alloys are being developed. The background for this thesis is to help find needed experimental data to calibrate and develop these model further. In this thesis the chosen material to study was from an extruded plate of AA6082 aluminium, which is a relevant material in for example the automobile industry.

Three different tempered cases has been studied in depth with Transmission Electron Microscopy, tensile tests and hardness curves. A hardness curve was made to find T6 which is the first case. The second case was weakly over aged at $185\,^{\circ}$C after reaching T6 until it reached $\approx 70\%$ of peak hardness. The third case was over aged at $200\,^{\circ}$C after reaching T6 until it also reached $\approx 70\%$ peak hardness. It has been made cross section area and length distributions of the precipitates for the three cases using a TEM. The tensile tests were done to relate the contributions of the different particle parameters such as length, cross section area and density to the mechanical properties of the material.

It was found in the tensile tests that the over aged materials experienced increased initial work hardening rate as compared to T6. The distributions showed that the material over aged at $200\,^{\circ}$C had wider and shorter precipitates compared to the material over aged at $185\,^{\circ}$C. It was also found that the over aged materials has a significantly lower particle density compared to T6.

Sammendrag

Det utvikles nye modeller for modellering av materialegenskapene til aluminiumslegeringer som tar hensyn til geometrien i nåleformede presipitater som kan bli funnet i 6xxx legeringer. Bakgrunnen for denne oppgaven er å bidra til å finne nødvendig eksperimentel data for å kalibrere og utvikle disse modellene videre. I denne avhandlingen er det undersøkte materialet fra en ekstrudert plate av AA6082 aluminium, som er et relevant materiale i for eksmpel bilindustrien.

Tre forskjellige utherdete tilfeller har blitt studert nøye med transmisjonselektronmikroskopi, strekktester og hardhetskurver. En hardhetskurve ble lagd for å finne T6 som er det første tilfellet. Det andre tilfellet er et svakt overeldet tillfelle som er utherdet på $185\,^\circ C$ etter å ha nådd T6 inntil den nådde *ca* 70 % av maksimal hardhet. Det tredje tilfellet var overeldet på $200\,^\circ C$ etter å ha nådd T6 før den også nådde *ca* 70 % av maksimal hardhet. Det har blitt funnet areal og lengde-fordelinger for presipitatene i de tre tilfellene ved bruk av en TEM. Strekkforsøk ble utført for å relatere bidragene fra de forskjellige partikkelparameterene som lengde, tverrsnittsareal og tettheten til de mekaniske egenskapene til materialet.

Det ble funnet av strekkprøvene at de overelda materialene opplevde økt initiale arbeidsherdingshastighet i forhold til T6. Lengde- og tverrsnittsarealfordelingene viste at materialet overelda på $200\,^\circ C$ hadde bredere og kortere presipitater enn materialet overelda på $185\,^\circ C$. Det ble også funnet at de overelda materialene har en vesentlig lavere partikkeltetthet enn T6.

Preface

This master thesis was written in the spring 2016 as the final part of my masters in Material Science and Technology at the Norwegian University of Science an Technology, NTNU Trondheim.

A lot of time was spent during this thesis on the experiments and especially on learning to operate and get good pictures using the Transmission Electron Microscope. This entire thesis has been very educational.

Table of Contents

List of Tables

List of Figures

Chapter 1

Introduction

The material used in this thesis was from a 15 years old extruded plate that was extruded for the VIRFORM Europear project in 2000-2004 [1], made of AA 6082 aluminium. The extruded plate is close to $3\,\mathrm{mm}$ thick and close to $20\,\mathrm{cm}$ wide and can be seen in **Fig. 1.1**. AA 6082 aluminium is an alloy that relies upon the strength gained from the precipitates formed in the aging process. Extruded and T6 tempered AA 6082 aluminium is very relevant for industry as it is being used for a lot, for example some components in the automobile industry and for bicycles. When the material is in service it is often at its peak hardness known as T6. In many cases the material might be exposed to heat when it is in use, such as the wheel suspension in some cars, that can be made from extruded and or forged 6082 aluminium. This will cause the material to over age and therefore lose some of the wanted material properties such as the hardness and the tensile strength. This thesis covers some tests done to see the effects of over aging after T6 because of its relevancy to the lifetime of the products in service.

The precipitates formed in this alloy are needle shaped, but the theoretical models that relates the precipitates in the material to the materials properties has until now assumed spherical precipitates[2]. A new model is being developed that can take the actual geometry into account [3] [4]. Therefore a lot of time has been spent using a Transmission Electron Microscope (TEM) to see the actual precipitates. The pictures has been used to find statistical distribution concerning the length, area and particle density of the precipitates.

Ultimately the goal has been to help find enough statistics of the relevant material parameters to further develop and calibrate an actual model that will take into consideration the geometry of the particles instead of just assuming them to be spherical. Such a model would be of great interest to the industry and these are some of the problems that when solved will help aluminium become even more relevant in today's market.

Figure 1.1: A picture of the extruded plate used in this thesis.

Chapter 2

Theoretical background

This chapter explains the needed theory for understanding the background and relevancy of this thesis and for understanding the discussion later on. The chapter also explains the equipment used for this thesis.

2.1 Aluminium

There are many advantages when it comes to choosing aluminium for the wanted application. First of all it is the most common metallic material in the earths crust [5], and when the material already has been produced it only takes about 5% of the extraction energy to recycle it, which is an important factor in the struggle of achieving a sustainable society. Secondly, even though pure aluminium is very soft, a lot can be done to strengthen it. Combined with the density of aluminium being approximately 1/3 of steel makes it very favorable when it comes to application for automobile industry and any industry where fuel efficiency is dependent on weight. The recycling factor alone makes it very advantageous for making one time use applications like soda cans.

Aluminium can be tailored to fulfill different roles and to organize the different alloys of aluminium and their properties it is first divided between wrought alloys and cast alloys. The second phase is separating again into heat-treatable and non-heat-treatable.

2.2 Precipitates and material

All the material used in this thesis came from the same extruded plate of AA 6082 aluminium. The 6xxx alloy series is a wrought alloy and is heat-treatable. After the material has been homogenized at $530\,^\circ\text{C}$ which is a process meant to evenly distribute the alloying components the material will be supersaturated with Mg and Si, then the material was extruded into the wanted shape.

The aluminium alloy AA 6082 contains magnesium and silicon and gets its strength from needle shaped precipitates formed during ageing[6]. Manganese is also present

to prevent recrystallization subsequent to solutionizing by pinning the grain boundaries, which is done by the manganese precipitates forming alpha dispersoids during homogenization. To be able to get these precipitates, the material is first solutionized to bring silicon and magnesium into solid solution, that will later help form the wanted precipitates by becoming supersaturated when the material is quenched. Silicon has a lower solubility and goes out of the solid solution and forms the Si-clusters at quenched positions. The magnesium will then diffuse towards these clusters. If the material is not quenched, but rather cooled down in room temperature, the desired precipitates will be lost as they diffuse into the equilibrium state called β-particles, which has is a Mg_2Si structure. After quenching, the material is age hardened, which causes Guinier-Preston zones (GP-zones) to be formed before the β" particles are formed [7].

The β"-particles are the wanted precipitates. They are the ones that will give the strongest material, as they are observed to occur at T6 [6]. β" precipitates will grow so that they are orientated in any of the <0 0 1>directions, which means they will block dislocations in any {1 1 1} slip plane. β" are meta stable particles approximately on the form Mg_5Si_6 and contains about 20% aluminium [8]. The β" particles has a monoclinic crystal structure, while the precipitates that are formed during the over aging will have a hexagonal structure [7][9][10]. Two models can be observed below, describing the characteristic shape of the β", **Fig. 2.1** illustrates the Mg_5Si_6 atomic sites for one formula unit. **Fig. 2.2** shows the β" cross section in an Al matrix, the yellow lines inside the precipitate indicate the monoclinic crystal, the yellow lines below show the directions of the edges in the Al matrix. The angle of the corner is $105.3°$, which can be used to identify the β" and distinguish them from other particles when doing particle distribution statistics[11][12].

Figure 2.2: A model of the β" position in the Al matrix with corresponding directions and angles. The monoclinic unit cell is also shown[11].

Figure 2.1: A simple model showing the atomic positioning in a β" particle with the formula Mg_5Si_6[11].

When the material becomes over aged, the β" particles will form other particles like B', β' and β, where as β is the equilibrium phase. There are two more discussed theories on how the over aged precipitates form from β", either they experience what is called on
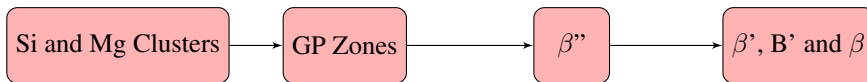
Figure 2.3: The progress of the hardening particles observed in 6082 aluminium.
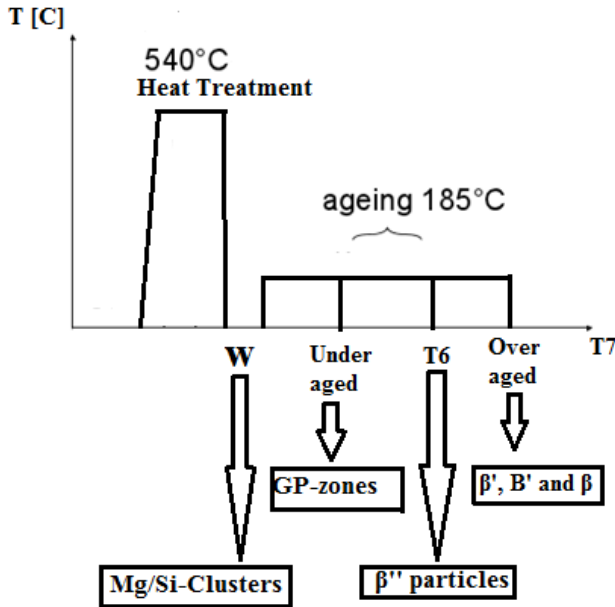
Figure 2.4: This figure shows the formation of the different phases and particles put into context of the heat treatment and the ageing process.

site transformation, where the β" just transform into β' and keeps transforming through the over aging. The other possibility is that β" dissolves, then nucleates and start growing as a β' somewhere else. **Fig. 2.3** and **Fig. 2.4** are two illustrations showing the formation order of the precipitates and when they appear in the ageing process. [13] [14]

The life cycle of the precipitates can be summed up with three main stages. The first stage is the nucleation, where solid Si forms Si-clusters because of its lower solubility. The next stage is the growth stage, now clusters form β" particles, then follows the order shown in **Fig. 2.3**. The growth is preferred in <0 0 1>in the aluminium matrix, and they grow as the Mg and Si diffuse to them from the supersaturated matrix. The final stage is the coarsening stage, at this point the nucleation stops as the matrix lacks solutes. To keep up the diffusion of Mg and Si the smaller precipitates dissolve to feed the bigger ones, reducing the total amount of precipitates.

The strengthening contribution from the precipitates comes from their ability to stop dislocations moving in the {1 1 1} slip plane, however the precipitates ability to stop these dislocation can happen in two ways, either the particle being in the way forces a

small part of the dislocation to glide through the atom planes of the precipitate that has a higher resistance to gliding, and this will cause disorder in the precipitates atom structure. When this happens the precipitate is called shearable. The other possibility is that it is too difficult to go through the precipitate, so the dislocation has to bypass the precipitate via the Orowan process, leaving behind a dislocation loop around the particle. The deciding factors for whether the precipitate is shearable or not is decided by the energy it takes for the dislocation to pass it, and this is decided from the coherency of the particle and internal resistance to dislocation glide inside the particle. A bigger cross section of the precipitate will result in a higher resistance, therefore it is possible to find an approximate critical cross section area of a type of particle that separates non-shearable and shearable precipitates. There is not a very high difference in the energy it takes for a dislocation to pass a shearable and a non-shearable precipitate close to the critical cross section area, the big difference is that the non-shearable precipitates will contribute to the work hardening because of the dislocation loops left behind from the bypassing dislocations. Hence the optimal precipitate will grow its diameter just big enough to become non-shearable, then only grow in length to block as many slip planes as possible.

Around the precipitates there might be a strain field that contributes to some degree to the strengthening of the material and is determined by how well the precipitates fit in to the aluminium matrix, this phenomenon is called coherency. **Fig. 2.5** shows the 4 different states of coherency. From the left, the first image shows a fully coherent particle which requires the particle to match the aluminium matrix in all directions. A fully coherent particle will therefore not bend any lattices, and not generate any strain. Second from the left shows a coherent particle, the spacing between the latices are different in the matrix and the particle, but the lattices are still continuous through the particle inn all directions. This spacing difference causes some strain in the matrix, which again causes some hardening. Third from the left shows a partially coherent particle, which is a mix of the previous two, some directions will experience a difference in the lattice spacing, while other directions match perfectly. This will yield some strain and cause a hardening effect. The last particle all the way to the right illustrates an incoherent particle, the lattices are not overlapping in any direction, and this causes minimal/no strain on the surrounding matrix, contributing very little to the hardness. For the first three cases a dislocation can chose based on least resistance whether to go through the precipitate or to by pass it. A dislocation can however not pass through an incoherent particle, only bypass it via the Orowan process. The β" particles prefer the <0 0 1>direction as they grow coherent in that direction and only semi-coherent in the other two directions as seen in **Fig. 2.6**, where red illustrates high strain and blue illustrates a low strain, causing them to give a strain field[11].

2.3   Modeling

The main goal behind this project is to help get all the values needed to create and calibrate more precise and accurate models [3][4]. This will help the industry to model the exact properties they want, but it will also help predict lifetime of components in use and how their properties will change. This can save money and prevent accidents from ever happening. Since modeling is so important, there are of course some models in use already, however most assume only spherical precipitates, which is not the case for 6xxx alloys.
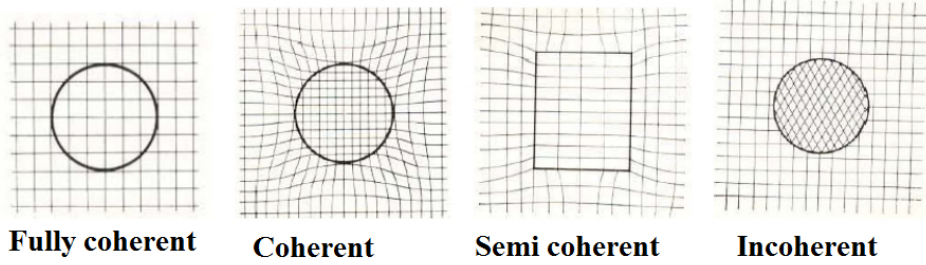
Figure 2.5: The 4 different types of coherency
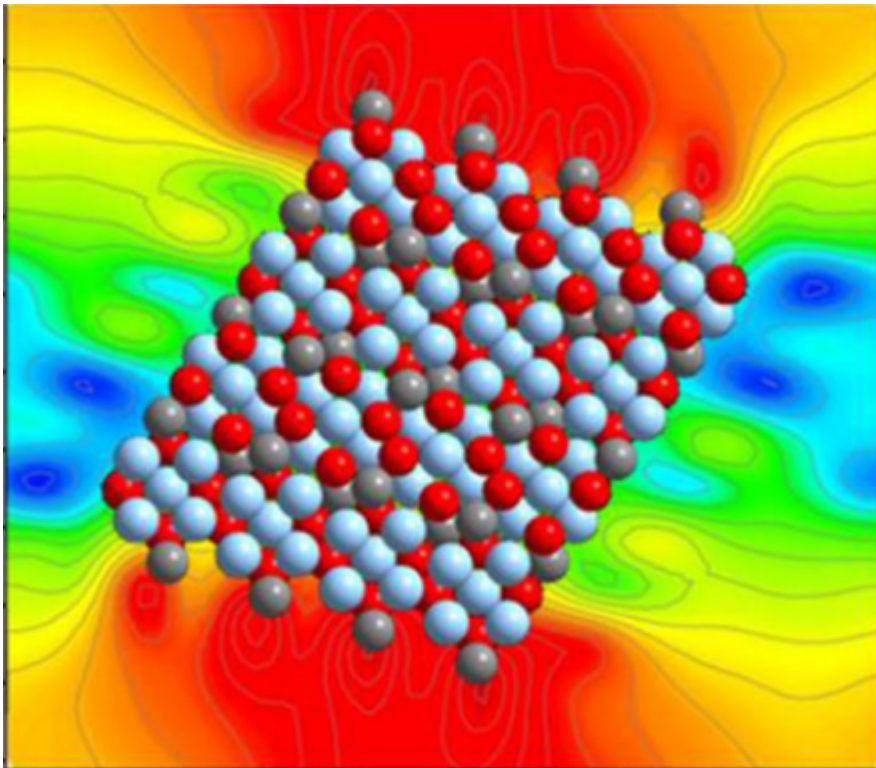
Figure 2.6: A strain field model around a β" precipitate showing high strain as red and low strain as blue.[11]

This is not accurate enough when the main contributors to the strength in the material are as shown the list below.

- The number of needles intersecting a slip plane.

- The statistical strength distribution as function of precipitate size.

- The spatial distribution of the precipitates.

This means needle shaped precipitates will have a higher strength contribution than a spherical one, since the needle shaped ones with the same volume as the spherical ones will intersect more slip planes, as is illustrated in **Fig. 2.7** below. This is assuming that the precipitates are non-shearable, meaning the mobile dislocations has to bypass the precipitates via the Orowan process rather than going straight through the precipitate, which is the case for thin shearable precipitates. Most of the precipitates in T6 are assumed non-shearable, and during the over aging all the precipitates are assumed to become non-shearable. Seeing how much of a difference the geometry of the precipitates will make on the strength contribution criteria listed above, one can understand why it is time for a better model accounting for needle shaped precipitates.
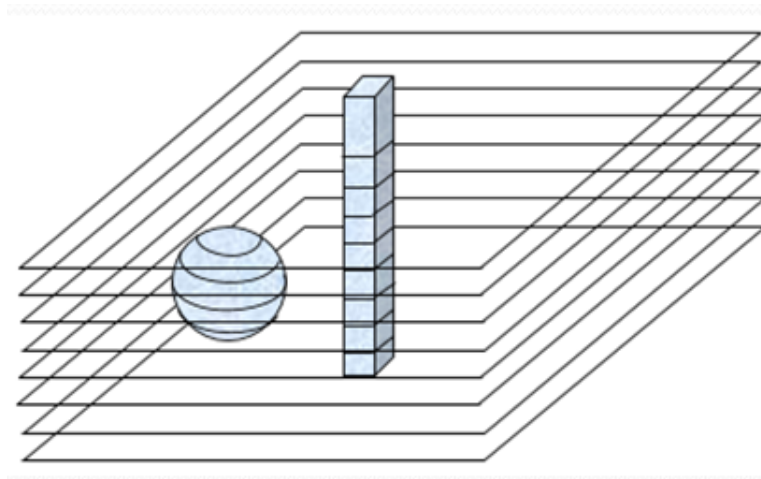
Figure 2.7: An illustration showing how needle shaped precipitates intersects more slip planes than a spherical one with the same volume.

Based on the particle size and geometrical shape distributions and the corresponding obstacle strength, a theory has been developed by Holmedal [15] to calculate the strength contribution from the precipitates. The model will not be derived here. The model takes account for the needle shaped precipitates piercing more slip planes than spherical ones. It needs statistical size distribution from either simulated or measured cases. The theory assumes all needle shaped particles have the average length and cross section area and that all the particles are evenly distributed in the material. For this case the particle contribution would be calculated from **Eq. 2.1**:

$$\sigma_p = 0.3 * M * \mu * b \sqrt{3 * \bar{l} * N_v} * f^{\frac{-3}{2}} * (1 - \frac{1}{6} * f^{-5}) \qquad (2.1)$$

Here M being the Taylor factor, μ, and b are known material parameters. $\bar{l}$ is the average length of the needle shaped precipitates, N_v is the statistical distribution of the number of particles per volume, and f the obstacle strength of the particles. To calculate f, a particle length distribution ϕ_l and a correlation function for the aspect ratio for particle $\Omega(\mathrm{l})$ is needed. This is mentioned to give an insight to what experimental data is needed, and why it is needed for the modeling.

2.4 Number density and Particle distribution

Another important parameter needed for the modeling is the number density (p_p), when measuring it, one applies a correction. The number of cross section particles times three divided by the volume would give an estimate larger than the actual density. The reason is the the volume that is being counted is larger than the actual picture area times the thickness, the reason being that only a fraction of the cross section precipitates would need to be inside the volume to be counted. To correct this the thickness of the counting volume is actually the average length of the precipitates larger than the measured thickness, which is simply because half the average length of precipitates is added to the top and bottom of the sample. **Fig. 2.8** illustrates how only a fraction of the cross section particles have to be inside the measured volume to still count, the red part is the part of the precipitates missing. The actual equation for finding the particle density is then as shown in **Eq.** (2.2). In the formula for number density (P_p), N is the number of cross section particles in the picture, which would represent $1/3$ of the total particles in the picture, t_s is the foil thickness, A_s is the sample area and l is the average precipitate length. [16] [17]

$$P_p = \frac{3 * N}{A_s * t_s (1 + \frac{l}{t_s})} \qquad (2.2)$$

2.5 Hardness curve

To find the time it takes to reach the different tempers, a hardening curve is made. The hardness curve is made by taking hardness tests at different stages during the ageing process. The chosen method of measuring the hardness was Vickers Hardness. Vickers Hardness [HV] is measured by a machine pushing a square-based pyramidal shaped diamond into the sample with a predetermined load. The hardness is then calculated by using the diagonals in the imprint as shown in **Eq. 2.3**. F is the load in Kg, the number 136°is from the angle of the lateral sides on the diamond and d_1 and d_2 are the diameters of the imprint. The curve will usually have a high slope the first minutes or hours as many precipitates gets stronger during the precipitate growth stage, then it will flatten out, reach a maximum which is T6, then it will decline steadily as the precipitates coarsen into strong particles, but becoming to few to uphold its hardness.
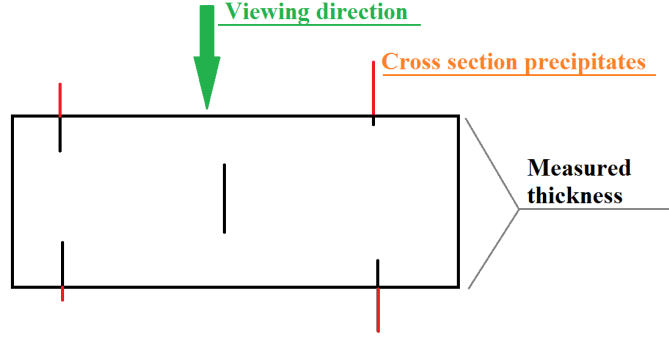
Figure 2.8: Shown why the need of a volume correction is needed for finding particle density.

$$HV = \frac{2 * F * sin(\frac{136°}{2})}{d_1 * d_2} \qquad (2.3)$$

2.6 Tensile tests

Tensile tests are done to give a stress/strain-curve, which will give useful information such as the E-modul, yield strength and the ultimate tensile strength. It is done by stretching the samples while measuring the force applied and the elongation. Using **Eq.** (2.4) and **Eq.** (2.5), a nominal stress (s) vs strain (e) curve is found. The true stress (σ) and the true strain (ε) curves can also be found using **Eq.** (2.6) and **Eq.** (2.7).

$$s = \frac{F}{A_0} \qquad (2.4)$$

$$e = \frac{\Delta L}{L_0} \qquad (2.5)$$

$$\varepsilon = ln(1 + e) \qquad (2.6)$$

$$\sigma = s(1 + e) \qquad (2.7)$$

Since σ and ε actually describes stress and strain at every moment, the equations above for σ and ε are not valid after necking occurs. This is because in the derivation of the equations, it is assumed that the length times area is constant. [18]

2.7 Transmission Electron Microscope

Very roughly, a Transmission electron microscope (TEM) works by sending an electron beam through a very thin part of a sample. The source of this beam is a filament, which in this case is a lanthanum hexaboride crystal (LaB_6), and with the Wehnelt cylinder that surround it they make up the electron canon. Then there are many of lenses guiding the electron beam as shown in **Fig. 2.9** and **Fig. 2.10**, and finally there is a fluorescent screen lighting up where it is hit by electrons. The lenses are not of traditional kind, but rather coils generating an electromagnetic field. The two main uses for the TEM are diffraction and microscopy. When a laser is spread in an optical grid, both constructive and destructive interference will happen in directions depending on the grid opening sizes. The same thing happens with the electron beam when it hits the atoms arranged in a crystal structure, and it is called diffraction. When looking at the diffraction patterns, it is important to be looking at smaller areas to observe only a single crystal direction, preventing a lot of background diffraction patterns from crystals with different orientations. A picture of the TEM used for this project can be seen in **Fig. 2.14**. [19]
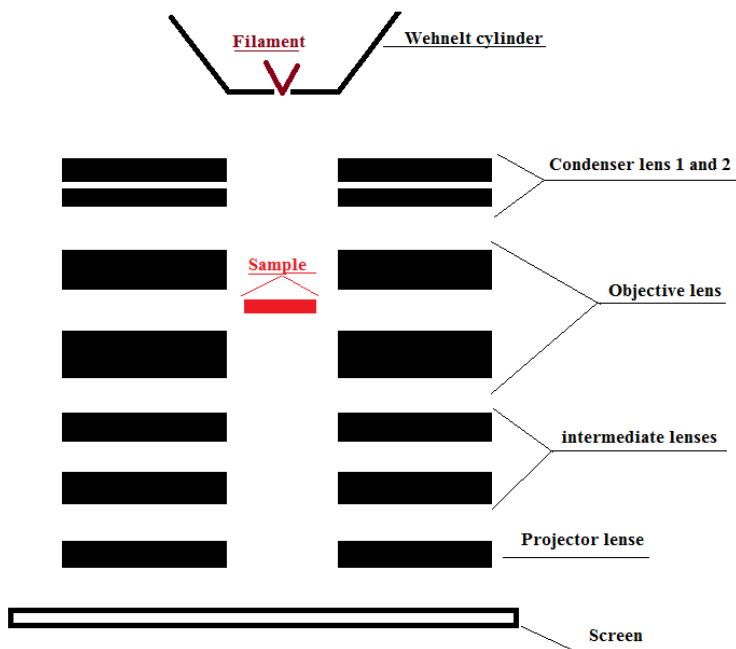
Figure 2.9: A basic description of the lenses in the TEM.
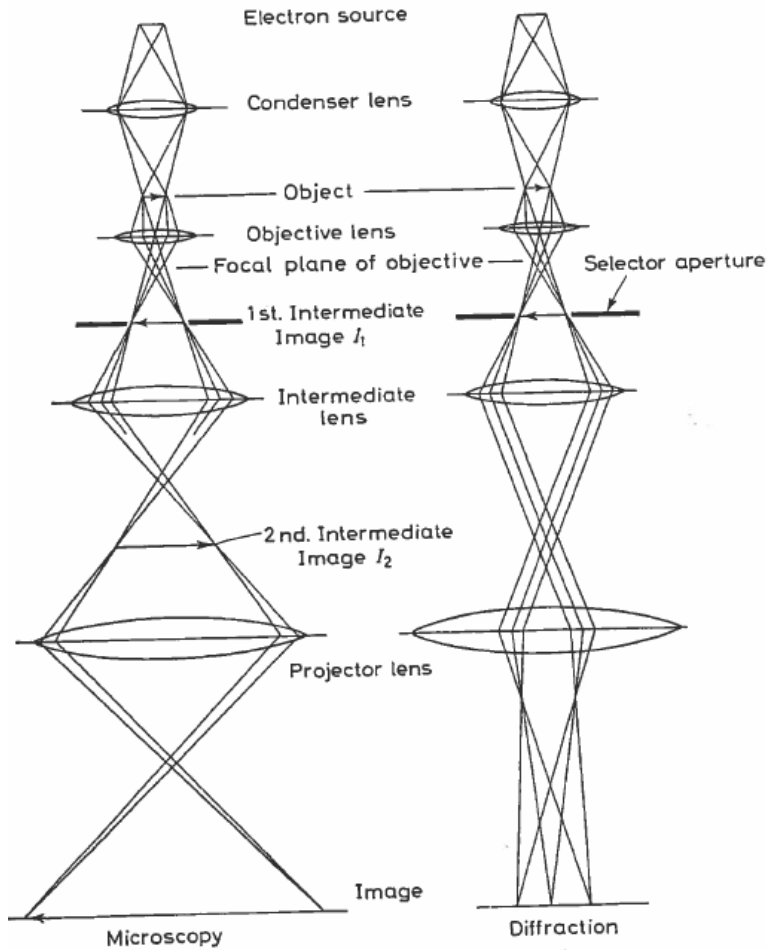
Figure 2.10: Difference between diffraction and microscopy electron path.

In this project the orientation of the sample has been crucial to get usable results, because to be able to see the full length of the precipitates one has to look at them top down in the [0 0 1] orientation, the diffraction pattern for [0 0 1] and several others one can encounter, is shown in **Fig. 2.11**. Finding the right orientation in a grain can be very time consuming and is done by checking the diffraction pattern, but usually the orientation is to far away from anything recognisable, which is when the Kikuchi lines are used. By centering the electron beam and switching to diffraction without using any diffraction aperture. A map of the Kikuchi lines are shown in **Fig. 2.12**.
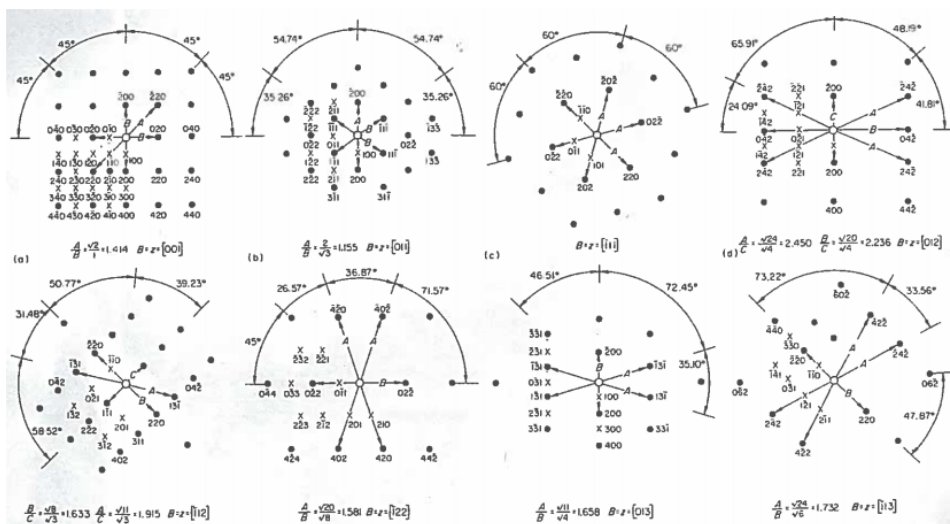
Figure 2.11: A map of how some of the diffraction patterns looks like in some orientations..
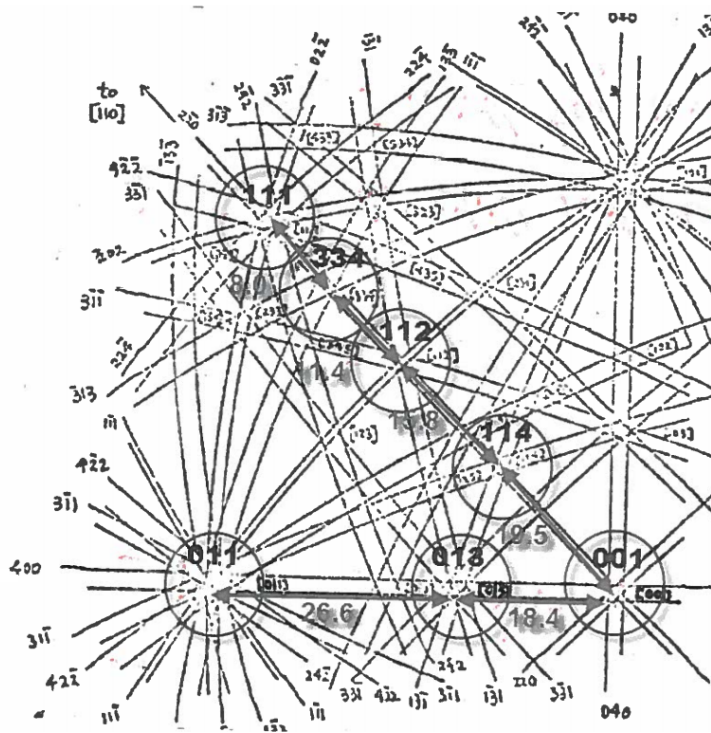
Figure 2.12: A map of the relevant Kikuchi bands and their orientations.
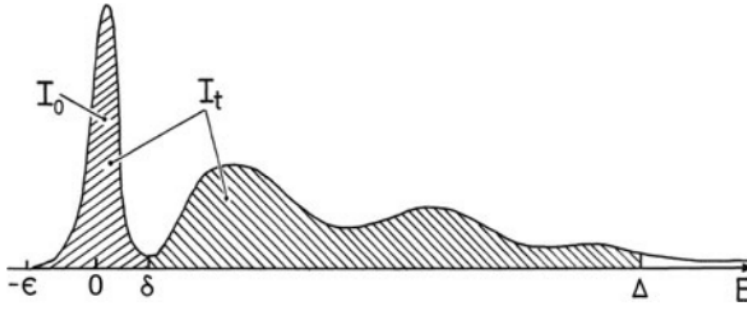
Figure 2.13: Example of low loss spectrum.

Another important part of TEM is Electron Energy Loss Spectroscopy (EELS), which is used to find the local area thickness of the TEM sample. It works by first recording a low loss spectrum as seen in **Fig. 2.13** which is an example of how it will look. The actual thickness is calculated using **Eq.** (2.8), where t is the thickness, λ is the total mean free path of all inelastic scattering and can generally be found for different materials in tables, however for this project an approximate λ value of $80\,\text{nm}$ was advised to be used from experience and knowledge by professors in the department. I_0 is the area under the zero loss peak, and I_t is the whole area under the low loss spectrum.

$$\frac{t}{\lambda} = ln(\frac{I_t}{I_0}) \tag{2.8}$$

In **Fig. 2.13** -ε and δ are the boundaries for the zero loss peak. A really rough description of what happens, is that some electrons go through the sample not being affected too much by the sample in way of energy loss as a result of the Coulomb attraction from the atoms, that is the zero loss, and is represented by the zero loss peak. Other electrons however are affected by a varying degree, and as seen from **Eq.** (2.8) this makes a lot of sense, as a thicker foil would cause I_t/I_0 to increase as less electrons would go through the sample unaffected. [20]

Figure 2.14: A picture of the TEM used in this project.

Chapter 3

Experimental procedures

This chapter describes the experimental procedures done in such a way that all the experiments should be easy to reproduce.

3.1 Hardness curves and finding the T6 parameters

In the beginning of the project, two different extruded plates were considered. The difference between them was the homogenization temperature. The homogenization temperatures were $580\,°C$ and $530\,°C$ respectively and it would be preferable to not have any recrystallization happen during the solutionizing since bigger grains gives a weaker material and is less relevant. Therefore samples were solutionized at $530\,°C$ for 30 minutes from both the plates to see if the grains would recrystallize. **Fig. 3.1** and **Fig. 3.2** shows the plate that was homogenized at $580\,°C$ before and after solutionizing respectively, and clearly shows some recrystallization, making it unfavorable. However **Fig. 3.3** and **Fig. 3.4** showing the material homogenized at $530\,°C$ before and after solutionizing respectively shows no signs of recrystallization, from which it was concluded to use that plate for this thesis. It can be observed that close to the surface of the samples, there is a recrystallized layer. This is a result from the strong shear deformation experienced in the extrusion process.
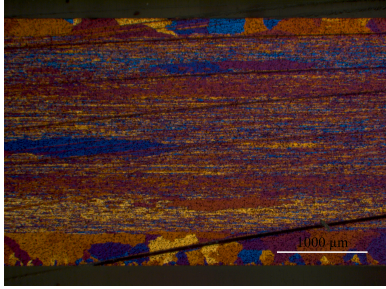
Figure 3.1: Light microscopy image of sample homogenized at $580\,^{\circ}$C, no solutionizing.
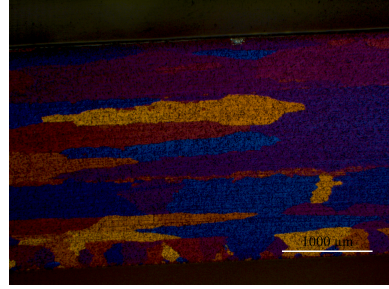
Figure 3.2: Light microscopy image of sample homogenized at $580\,^{\circ}$C, with solutionizing. Recrystallization can be observed.
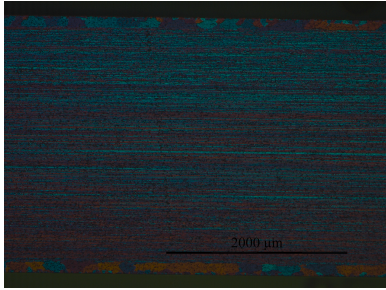
Figure 3.3: Light microscopy image of sample homogenized at $530\,^{\circ}$C, no solutionizing.
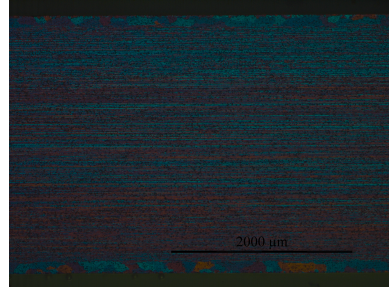
Figure 3.4: Light microscopy image of sample homogenized at $540\,^{\circ}$C, with solutionizing. Can observe no recrystallization.

T6 is the temper that corresponds the hardening time yielding peak hardness. To find the amount of time required to obtain T6 for the material, a hardening curve was made. A hardening curve shows the material's hardness vs the time spent age hardening.

30 mm was cut of from both sides along the extrusion direction of the given extruded plate to prevent any source of error from the plate not being transversely homogeneous, since the sides of the extruded plate might have experienced a different deformation mode than the rest of the plate. Some samples were cut from the remainder of the plate and grinded by discs of different grit size, the lower the grit size of the particles on the plate the smoother it is, resulting in a smoother surface of the samples. The plates used for grinding the samples for hardness testing were 800 and 1200 from the Federation of European Producers of Abrasives (FEPA) standard. Then samples were all solutionized at $530\,^{\circ}$C for 30 minutes, then put in an oil bath at 185°C. The samples were taken out and hardness tested at different times. The parameters for the hardness test are listed in **Table. 3.1**. This gave the hardening curve shown in **Fig. 3.5**.

Table 3.1: Hardness test parameters

Pressure	$1\,\text{kPa}$
Load time	$15\,\text{s}$
Loading speed	$100\,\mu\text{m}\,\text{s}^{-1}$
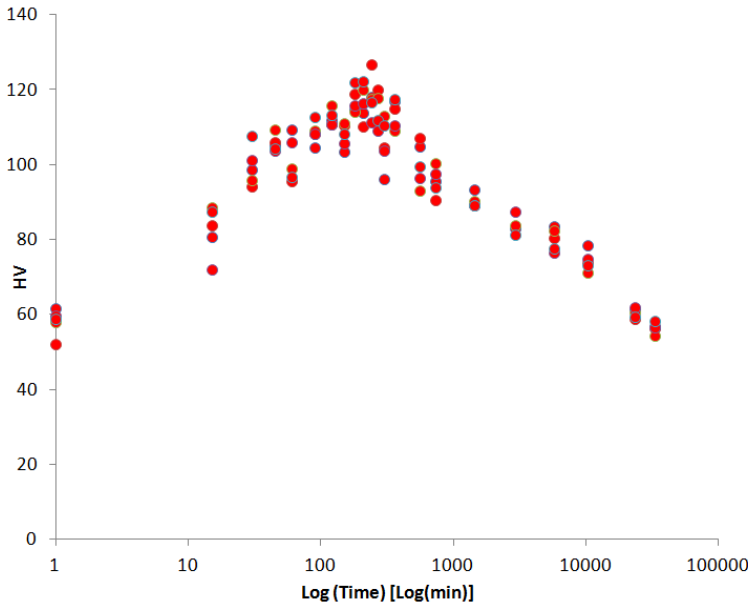
Figure 3.5: 5 tests were taken per sample, all results are shown in this graph

From this result T6 was found to occur at approximately 4 hours, therefore the parameters for the material were chosen to be 30 minutes of solutionizing at $530\,°\text{C}$, then quenching and finally 4 hours of age hardening at $185\,°\text{C}$ before the last quench. This matches with the expected heat treatment to obtain T6 [1].

Parallel to this, some samples had been taken out at exactly T6 and switched to another oil bath holding 200°C. These samples were similar to the others in every way other than the fact that they age hardened at $200\,°\text{C}$ after reaching T6 at $185\,°\text{C}$. The temperature was checked every time a sample was tested to minimize sources of error.

Due to the time limitations of this thesis, only three cases was chosen to study in depth with tensile tests and in TEM. The three cases are as shown in **Table. 3.2**.

Case number	% peak hardness	Time over aging after T6	Temperature [°C] after T6
1, T6	100%	–	–
2, over aged	70%	44 hours	185
3, over aged	70%	9 hours	200

Table 3.2: Case descriptions. All have been solutionized at 530 °C C for 30 minutes.

3.2 Tensile testing

Samples of the extruded plate were prepared in the workshop with the specifications shown in **Fig. 3.6**. The samples were heat treated as shown in **Table. 3.3**.

Sample number	Hours age hardening	Temperature [°C]
1-3, T6	4	185
4-6, over aged	48	185
7-9, over aged	9 after T6	200
10-12, Only solutionized	–	–

Table 3.3: Tensile test descriptions. All have been solutionized at 530 °C for 30 minutes.

12 samples were made in total, so for each of the 4 tests performed, 3 parallel tensile test samples were used to lower the sources of error. Samples 10-12 were only solutionized, this means they were taken out of the salt bath and quenched then stretched as soon as possible afterwards. It was consistently used between 5-8 minutes between quenching and the start of testing. This is because right after solutionizing the samples are very unstable. All samples are stretched at the rate of $2\,\mathrm{mm\,min^{-1}}$.
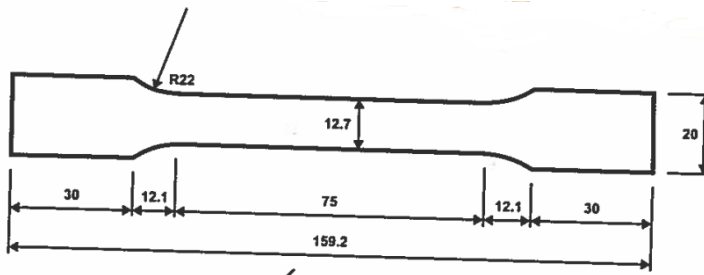
Figure 3.6: Tensile test sample measurement, all measurements are in mm.

3.3 Preparation of TEM samples

A lot of samples were cut from the plate and heat treated to the three different cases, for then to be made into TEM samples. The samples had roughly the size between $10\,\text{mm} \times 10\,\text{mm}$ and $20\,\text{mm} \times 20\,\text{mm}$. It was always made at least 4 samples, since some of them would usually be destroyed during the mechanical grinding. Making TEM samples starts by griding the samples down to the thickness of $100\mu m$ by hand. This is done by fastening the samples to a straight square of hardened epoxy, using double sided tape to keep the samples from becoming skew and bended when being grinded. The samples are grinded on the disc roughness of 320, 500, 800, 1200 and 2000 FEPA standard on each side, resulting in the TEM samples always coming from close to the middle of the plate, as shown in **Fig. 3.7**, which is very preferable, as it makes sure the recrystallized layer close to the surface is avoided. When grinding on 1200 and 2000 it is important to use soap to lower the friction. This process takes a lot of practise, and several of the samples were lost simply because they were grinded away completely, as shown in **Fig. 3.8**.

3mm thick

TEM Sample

Area from where the TEM samples are made, about +/- 1mm from the middle of the sample.

Original sample to be made TEM samples of
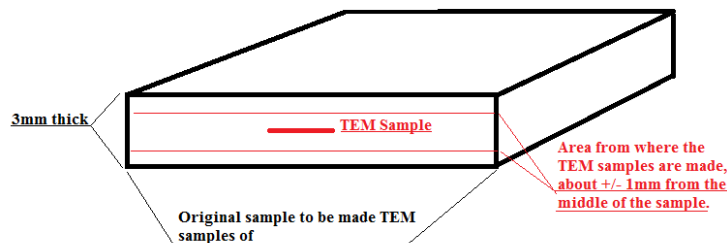
Figure 3.7: A description of where the TEM samples come from related in the extruded plate.
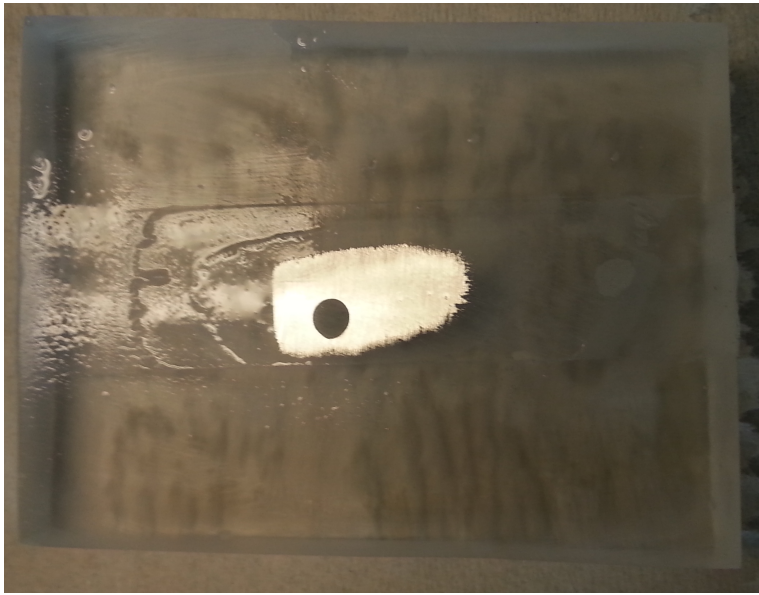
Figure 3.8: The sample was $20mm^2$ before grinding, but on the picture it is about $4*8mm^2$ and not homogeneous enough to make any samples from.

When the samples were about $100\mu m$ thick, they were removed from the tape by using liquid nitrogen. This destroys the adhesive properties of the tape, and then by using a scalpel, the samples were removed with as little damage as possible. Any tape residue is removed by cleaning the samples in acetone and rubbing extremely carefully with cotton.

Finally the samples are punched out of the aluminium foil in a circular shape with 3mm in diameter as shown in **Fig. 3.9**, one foil can give between 10-30 TEM samples, and then electropolished using the setup shown in **Fig. 3.10**. The electrolyte is in the white container and is a mixture of $600\,\mathrm{ml}$ methanol and $300\,\mathrm{ml}$ HNO_3, the sample is placed in a device that holds it in place while still exposing as much as possible of the surface to the electrolyte. In front of the sample there is a light source, and in the back there is a detector. The sample is done when the detector detects as much light as was programmed before starting the procedure. The sample is then quickly removed and cleaned in methanol to stop the sample from etching further. The sample is then removed from the holder, and cleaned in another container of methanol, before it is finally rinsed in ethanol. The samples are then put into individual pill casings as shown **Fig. 3.11**.
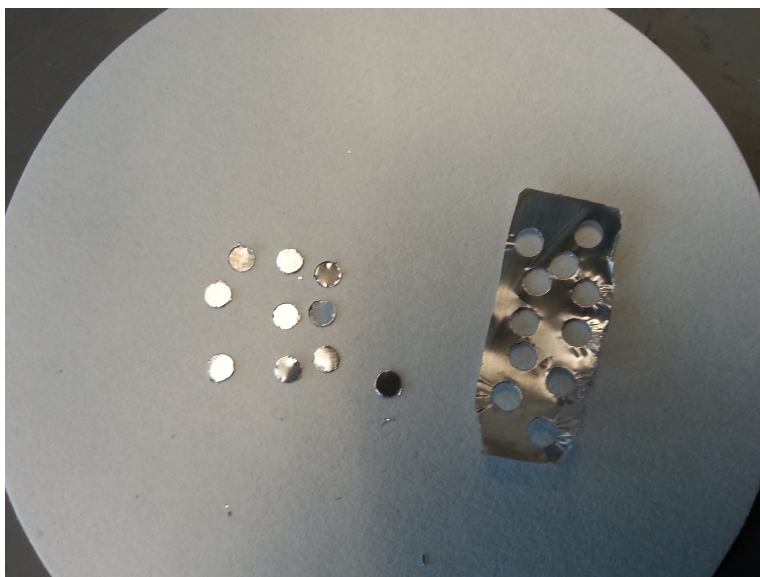
Figure 3.9: The samples are 3mm across. This is right before electropolishing.
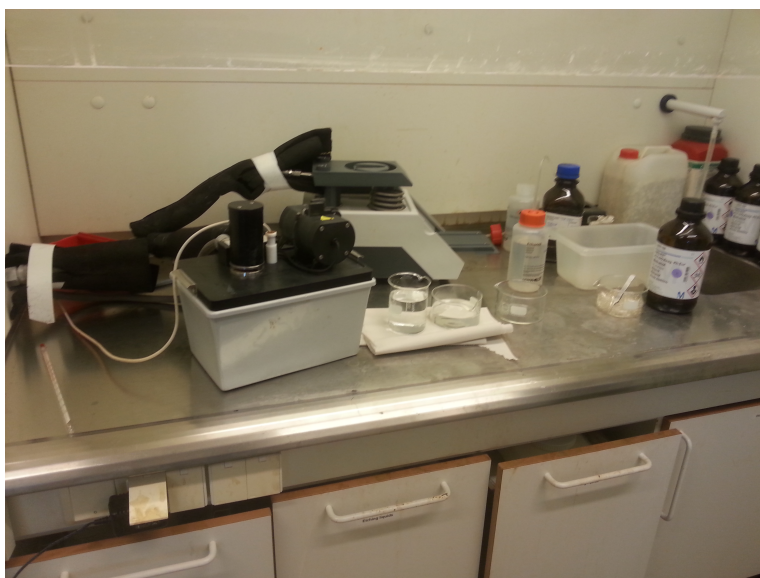
Figure 3.10: Electropolishing setup. The white box contains the electrolyte, the two beakers on the left both contain methanol and the beaker to the right contains ethanol.
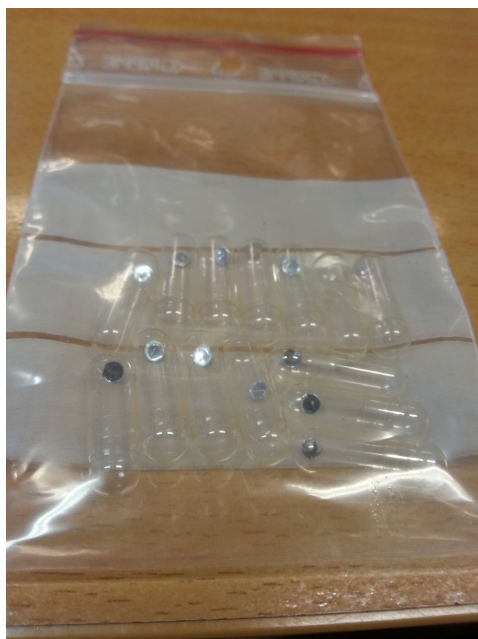
Figure 3.11: Each of the TEM samples are in individual pill casings, and are ready to be observed in the TEM.

3.4 TEM

Originally the plan was to use a Jeol 2010, but the filament was too old and the Gatan Image Filtering (GIF) was not working. Therefore a Jeol 2100 located in the basement of chemistry block I was used instead. The goal was to take pictures showing a good representation of length distribution, particle distribution and particle density. It was done by finding a thin part of the sample close to the electropolished hole, and finding a grain that could be tilted to find the [0 0 1] direction. Usually if the sample was tilted more than $10°$, it was a lot more difficult to get a whole picture in focus. For all the pictures taken, there was also done Electron Energy Loss Spectroscopy (EELS) to measure the local thickness of the sample where the picture was taken. A lot of pictures was taken from the 3 cases that was chosen to study, but due to the nature of TEM which is demanding a lot of practice and experience, there is a some difference in quality of the pictures taken that will yield some source of error.

Chapter 4

Results

This chapter will show all the results found from the experiments done, and some basic observations done from these results.

4.1 Hardening curve

From the hardness measurements shown in **Fig. 3.5** T6 was identified, but in **Fig. 4.1**, it is also shown the hardness curve that was made for the material over aged at $200\,°C$. **Fig. 4.1** shows how the over aged material loses its hardness relatively fast after T6. The samples that were over aged at 200°C lost their hardness quicker than the samples at $185\,°C$, even though the temperature difference was only 15°C. After 44 hours of over aging after T6, the samples in 185°C have a hardness somewhere between 83-86 HV, which is $\approx 70\%$ of peak hardness. To achieve the same hardness at $200\,°C$ after T6, it only took 9 hours, which is just 20% of the time it took at $185\,°C$. These cases are interesting to study, as they have the same hardness achieved at different temperatures, which might result in different distributions, length, area and density of particles. The actual hardness measurements are given in **Table. 4.2** and **Table. 4.1** for 185°C and 200°C respectively.
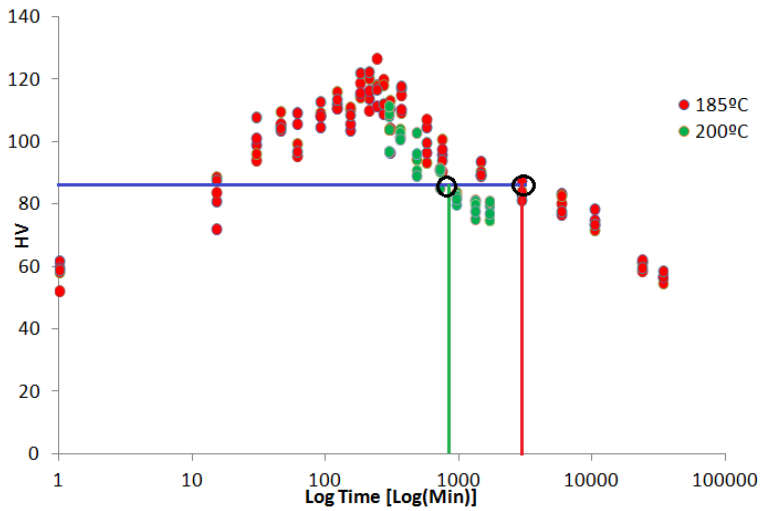
Figure 4.1: The entire hardening curve. Finding the 70% peak Hardness for 185 °C and 200 °C to be 44 hours and 9 hours after T6 respectively

Table 4.1: Hardness for material aging at 200°C.

Time aging [Min]	Hardness (HV)				
300	104.0	108.4	108.9	111.3	97.2
360	104.0	102.1	101.4	102.8	100.9
480	94.3	96.5	102.7	90.8	89.2
600	101.0	97.4	99.4	99.8	97.2
720	91.6	91.1	85.2	90.2	91.4
960	83.8	80.2	82.6	82.4	81.8
1320	81.4	81.1	75.3	79.8	78
1680	74.9	79.8	81	74.9	77.3

Table 4.2: Hardness for material aging at 185°C. *Only the 30 minutes solutionizing done to this sample.

Time aging [Min]	Hardness (HV)				
0*	61.7	52.1	58.1	59.6	59.0
15	80.9	83.8	88.8	72.2	87.6
30	98.8	94.2	96.1	101.2	107.7
45	105.1	105.8	109.6	105.7	109.4
60	109.4	95.6	99.2	105.9	97.0
90	104.7	108.1	109.2	108.2	112.8
120	112.0	111.7	116.1	110.9	113.5
150	103.6	110.4	111.1	105.6	108.4
180	114.8	118.9	114.3	115.7	122.2
210	113.9	110.2	120.2	116.4	122.4
240	118.1	126.7	117.6	111.4	116,8
270	111.4	120.0	117.9	109.1	112.0
300	96.3	104.5	113.2	103.9	110.7
360	117	115	109.2	110.4	117.7
560	104.8	107.1	93.4	96.4	99.8
740	95.7	90.4	100.6	97.5	94.2
1440	93.5	89.1	90.4	89.3	89.4
2910	83.1	68.8	84.1	87.4	81.4
5790	83.5	80.4	82.6	76.7	77.8
10350	78.5	73.6	71.5	74.9	73.4
23400	61.4	58.7	60.8	62.0	59.6
33360	56.9	56.4	54.6	56.7	58.4

From the hardness measurements two other cases were chosen to study at about 70% of peak hardness over aged at $185\,°C$ and $200\,°C$. They were found to be at 44 hours and 9 hours of aging after T6 respectively. this can be seen in the **Fig. 4.1**. Also the hardness of the 70% peak hardness cases were checked on the samples before they were made into TEM samples, to verify that they were close to 70% peak hardness. The hardness can be seen in the list below.

Table 4.3: Hardness at the two 70% peak hardness cases before the samples were made into TEM samples.

| Case	Hardness (HV)				
Case 2: $185\,°C$ 44 hours after T6	85.6	85.0	83.9	85.5	85.9
Case 3: $200\,°C$ 9 hours after T6	85.9	87.1	85.2	84.8	84.4

The average of these are 85.2 and 85.8 for 44 hours and 9 hours respectively. The average of T6 is 118. So the two cases are both 72% of peak hardness. This results in the cases shown in **Table. 4.4**.

Table 4.4: Description of the three cases

Case	Description
Case 1	T6. 100% peak hardness
Case 2	$\approx$ 70% of peak hardness achieved with over aging at 185 °C for 44 hours after T6
Case 3	$\approx$ 70% of peak hardness achieved with over aging at 200 °C for 9 hours after T6

4.2 Tensile tests

Fig. 4.2 shows all the nominal stress/strain-curves given from the tensile tests and **Fig. 4.3** shows all samples after they were stretched. In **Fig. 4.3** samples 1-3 are at T6, samples 4-6 are case 2 T6+44h 185 °C, samples 7-9 are case 3 T6+9h 200 °C and samples 10-12 are the solutionized samples. It is observed from the picture that sample 3 had its fracture close to the edge, causing it to be right outside the range of the extensometer. Samples 4-6 and 7-9 are all good, even though samples 4 and 8 had their fractures a little too close to the edge. Samples 10-12 all had their fracture close to the edge and they are all notably more elongated than the rest, which fits with the graphs.
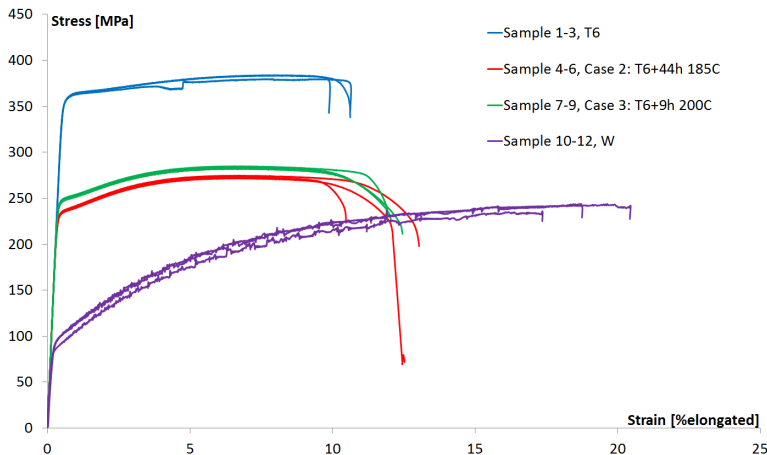
Figure 4.2: As mentioned in **Table. 3.3**, samples 1-3 are at T6, samples 4-6 are age hardened to T6 then over aged for 44 hours at 185°C, samples 7-9 are age hardened to T6 then aged for 9 more hours at 200°C, and samples 10-12 are taken directly from the solutionizing. They are all nominal stress/strain-curves
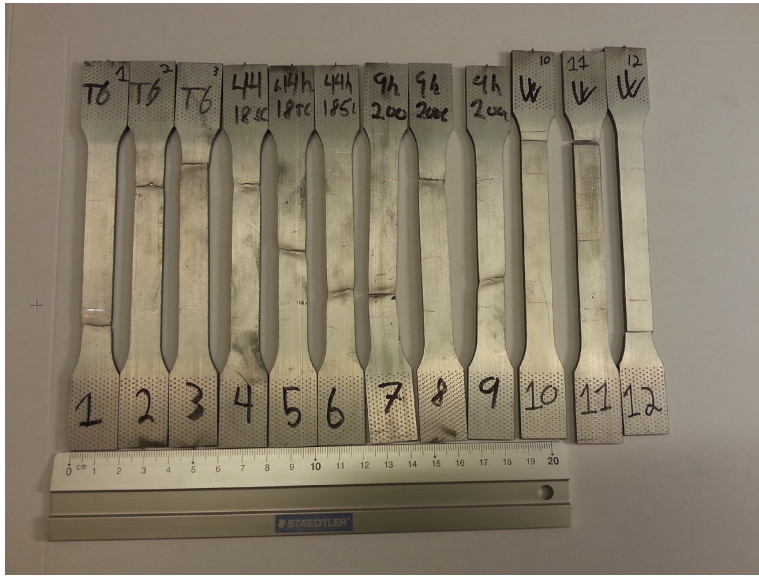
Figure 4.3: All tensile test samples after testing marked with their sample number.

Fig. **4.2** shows all the nominal stress/strain-curves in the same image, and from that it is easy to see that the T6 samples 1-3 [Blue] has the highest yield strength, second comes the samples 7-9 [Green] which were aged at $200\,°C$ for 9 hours, then comes the samples 4-6 [Red] which were aged at $185\,°C$, and finally only the solutionized samples 10-12 [Purple]. It shows that samples 10-12 are by far the the most ductile, as they were elongated to about 20%. Since case 2 (samples 4-6) and 3 (samples 7-9) has the same hardness, it was expected for them to have very similar stress/strain-curves, and it was also expected for T6 to have the highest yield strength. In **Fig. 4.4** there is a sudden drop in sample 1, this is a result from the sample not being fastened well enough during the tensile testing. Even though the Elastic zone looks very close to sample 2 and 3, the results from sample 1 will be discarded.

The nominal stress/strain-curves for samples 4-6 and 7-9 are very similar as seen in **Fig.** (4.2). Samples 7-9 which was aged at $200\,°C$, are slightly above samples 4-6 which were over aged at $185\,°C$. This can also be seen in **Table. 4.5**, showing that case 3 has a slightly higher ultimate tensile strength. The fact that it is only slightly higher might indicate some source of error during either the testing or more likely during the aging process.

Using **Eq.** (2.6) and **Eq.** (2.7) to find σ and ε, the graphs for true stress and true strain has been plotted below. The equations for finding σ and ε are not valid after the material starts necking since the equations rely on the volume preservation and therefore the area being kept homogeneous. **Fig. 4.5** shows all the σ/ε-curves for samples 2-12. Again the yield strength and ultimate tensile strength is considerably higher for T6, case 3 (sample 7-9) is slightly higher than case 2 (sample 4-6).
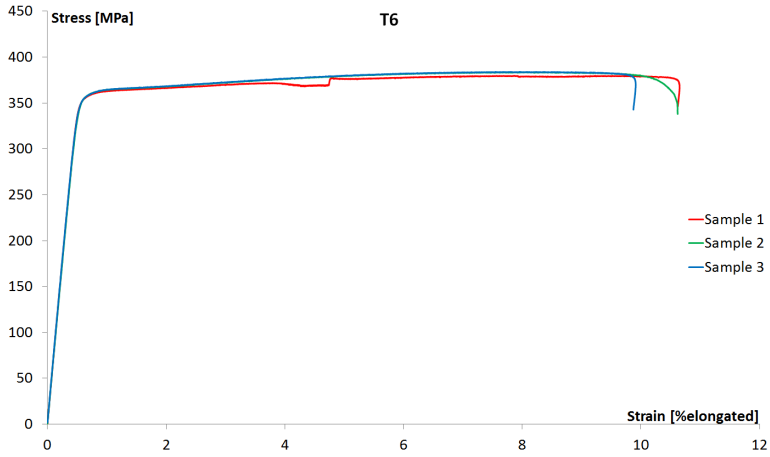
Figure 4.4: nominal stress-strain curve for samples 1,2 and 3.
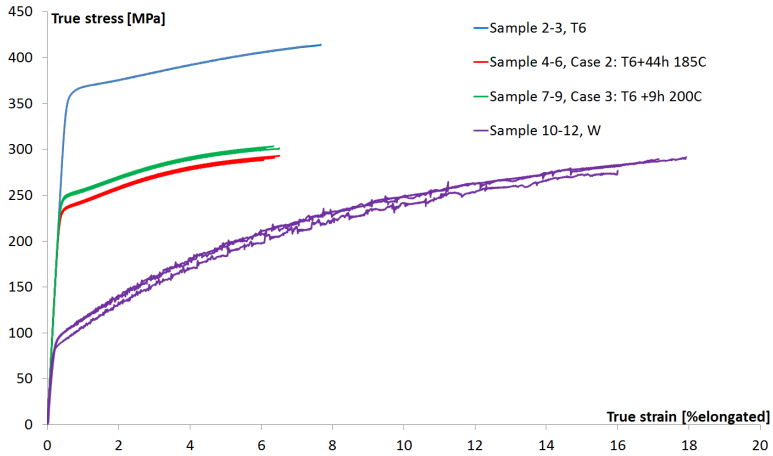
Figure 4.5: True stress/strain-Curves.

The important values from these tests are the yield strength, the ultimate tensile strength (UTS) and the E-module, which have all been calculated in **Table. 4.5** below. The E-module is the slope of the curve where the sample only experiences elastic deformation, and is therefore found by dividing $\Delta\sigma$ on $\Delta\varepsilon$ in the elastic area. The yield strength found is the 0.2% offset yield strength, and it was found by making a line with slope of the corresponding E-module that will intersect elongation (stress = 0) in 0.2% and checking when the line intercepted the stress-strain curve. UTS is the stress registered at the highest load. No values are fund for sample 1, because of the problems previously discussed.

Table 4.5: Tensile test values

Case	Sample	Yield strength 0.2% [MPa]	UTS [MPa]	E-Modul [GPa]
T6	1	-	-	-
	2	359.8	383.7	70.7
	3	360.1	384.1	70.6
Case 2 T6+44h 185 °C	4	236.3	273.3	70.1
	5	235.6	271.8	71.4
	6	236.0	274.8	72.4
Case 3 T6+9h 200 °C	7	248.6	283.8	73.1
	8	250.5	284.9	72.0
	9	247.1	282.5	72.9
W Only solutionized	10	86.4	236	65.4
	11	95.2	243.9	63.7
	12	94.9	243.9	65.8

These values confirm our analysis of **Fig. 4.2** with all the tensile test together. Samples 2 and 3 are the ones with the highest yield strength and samples 10-12 has the lowest. The E-module is stable at around 70-73GPa except for samples 10-12 who were only solutionized. They have a much shorter elastic zone, which makes it more susceptible to errors in finding the E-module, but also they are observed to be slightly less steep than the others.

4.3 TEM pictures

The following pictures are just the ones that where directly used for measuring and counting statistics. The Electron Energy Loss Spectrum is shown for each of the pictures used for finding particle density.

Fig. 4.6, **Fig. 4.7** and **Fig. 4.8** are pictures proving the right orientation of the samples, and can be compared to **Fig. 2.12** and **Fig. 2.11** to see that the [0 0 1] orientation has been achieved.
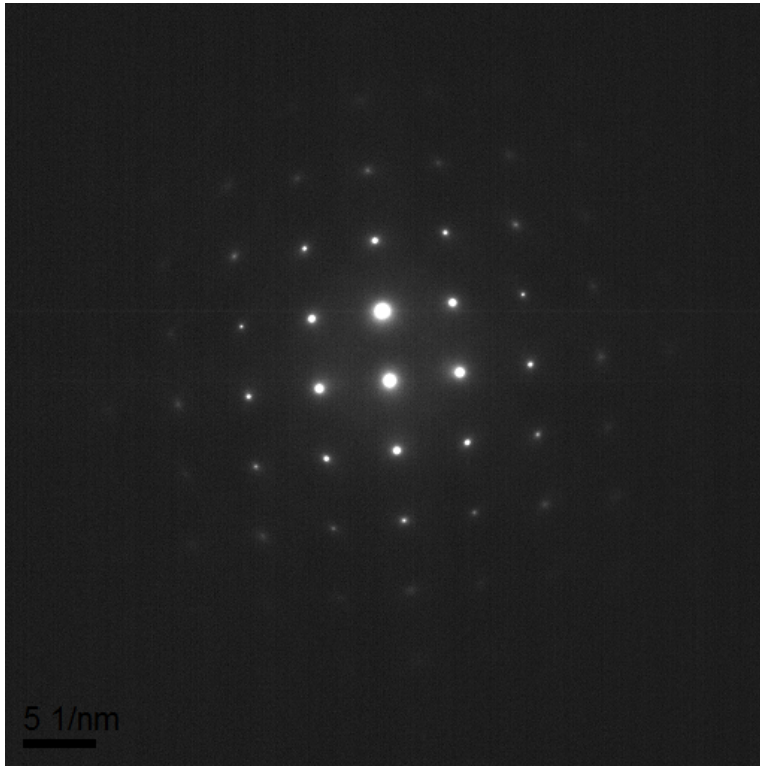
Figure 4.6: The diffraction pattern achieved when obtaining the [0 0 1] orientation.
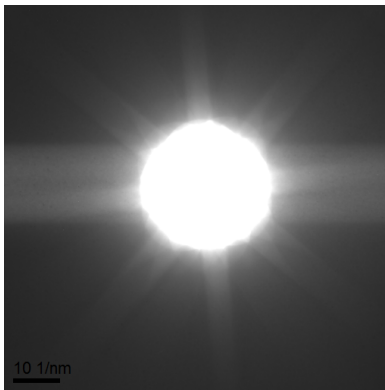
Figure 4.7: Kikuchi bands
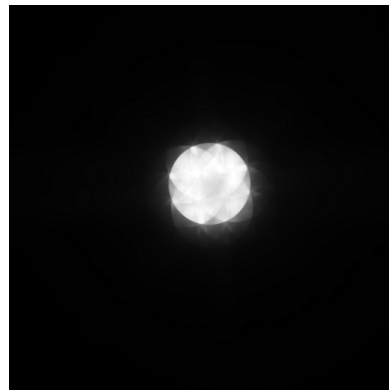
Figure 4.8: The cross section of the Kikuchi bands in focus for [0 0 1] orientation

Fig. 4.9 shows an overview of the grain where **Fig. 4.10** and **Fig. 4.11** were taken. This is at T6, and **Fig. 4.10** shows the picture that was used for statistical analysis on particle length, area and density. **Fig. 4.11** shows the highest resolution achieved in this thesis,

and it is to some extent possible to see the atom arrangement of the precipitates. **Fig. 4.12** shows the EELS for **Fig. 4.10**, which is used to find the thickness of the sample exactly where the picture is taken. Last there is **Fig. 4.13** showing a picture of a precipitation free zone along the grain boundary at T6.
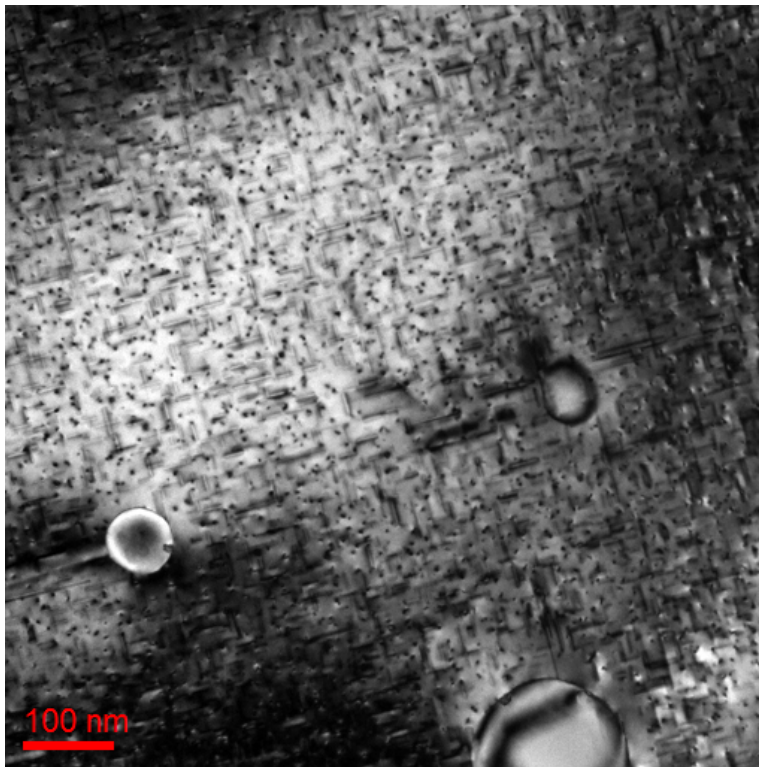
Figure 4.9: T6. Overview of the grain where **Fig. 4.10** and **Fig. 4.11** were taken..
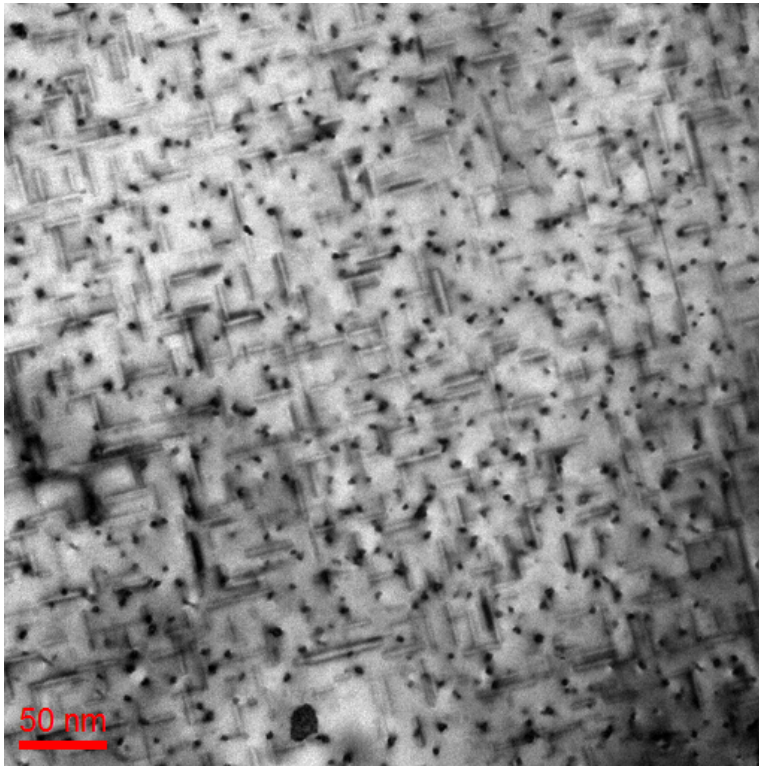
Figure 4.10: The picture used to find statistics for T6.
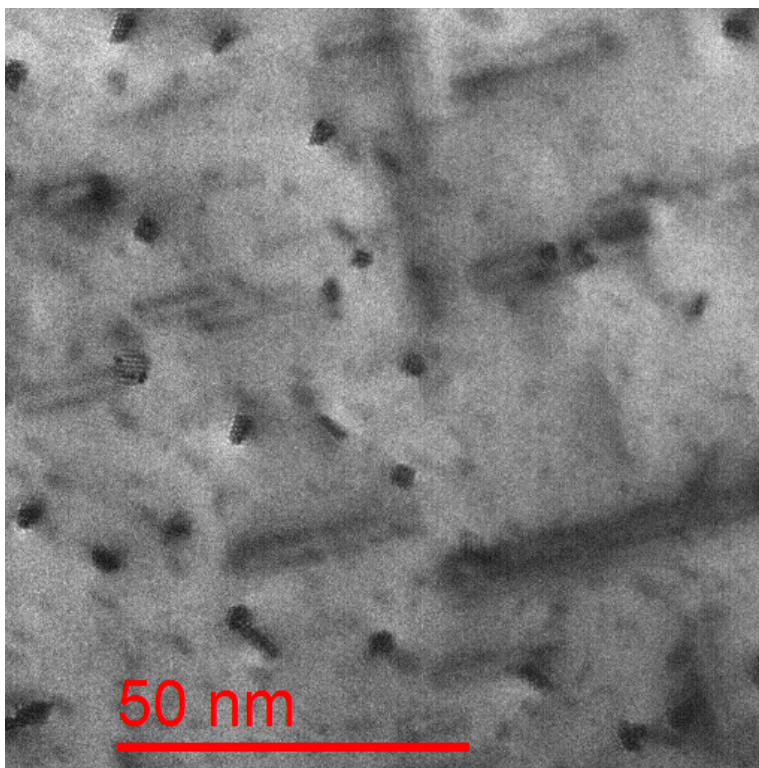
Figure 4.11: A high resolution image for T6 showing some atom arrangement.
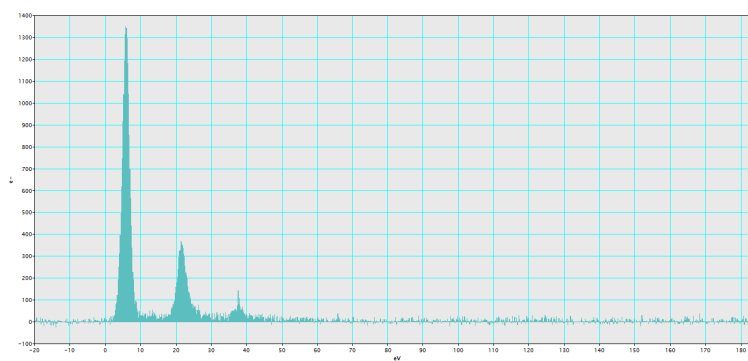
Figure 4.12: Electron Energy Loss Spectroscopy for **Fig. 4.10**.
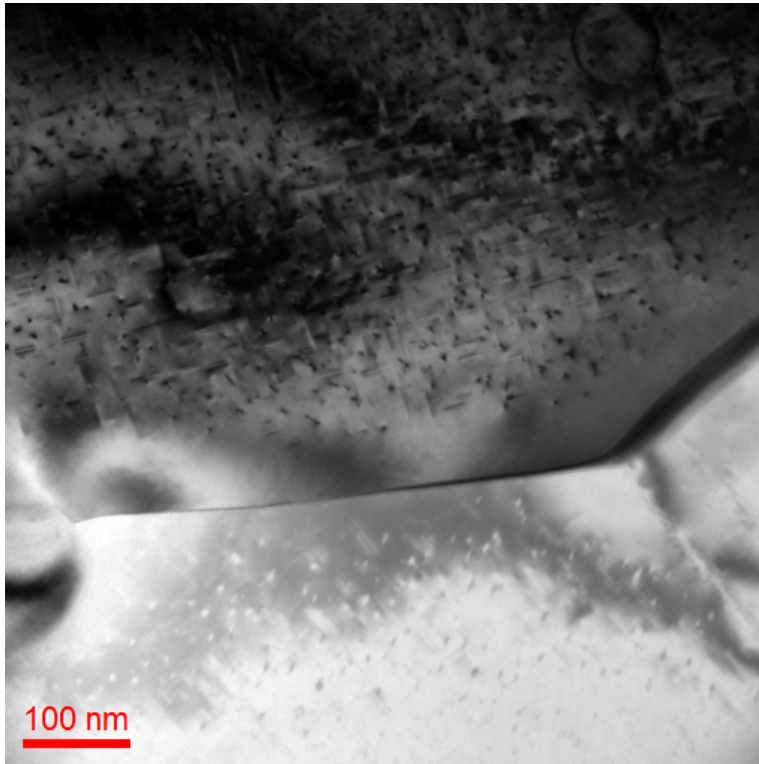
Figure 4.13: An image showing the precipitate free zone close to the grain boundary.

Fig. 4.14 is the picture used for finding statistics for case 2, over aging at $185\,°\text{C}$. **Fig. 4.15** is the EELS for **Fig. 4.14**.
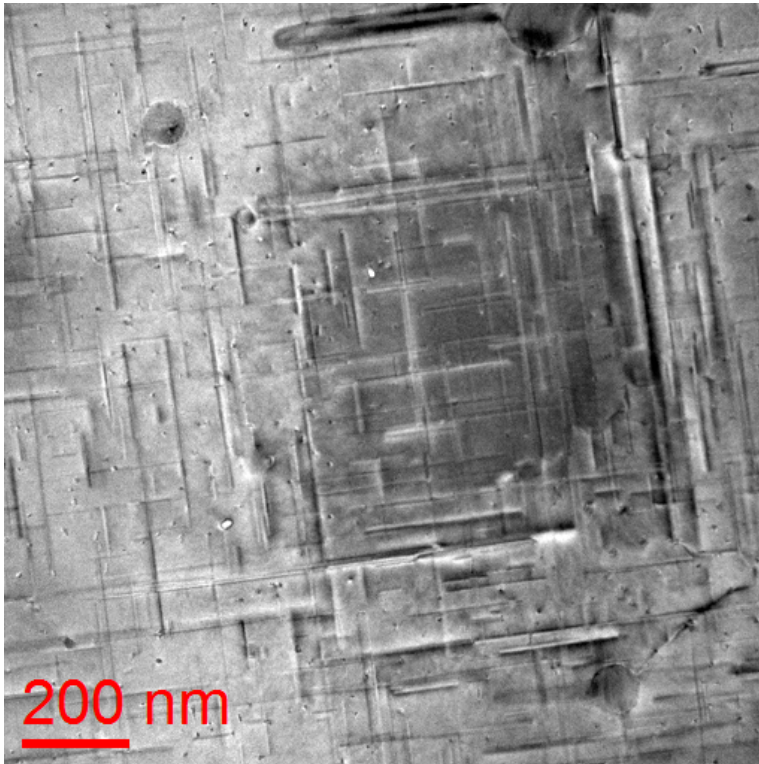
Figure 4.14: Picture used for finding statistics for case 2 .
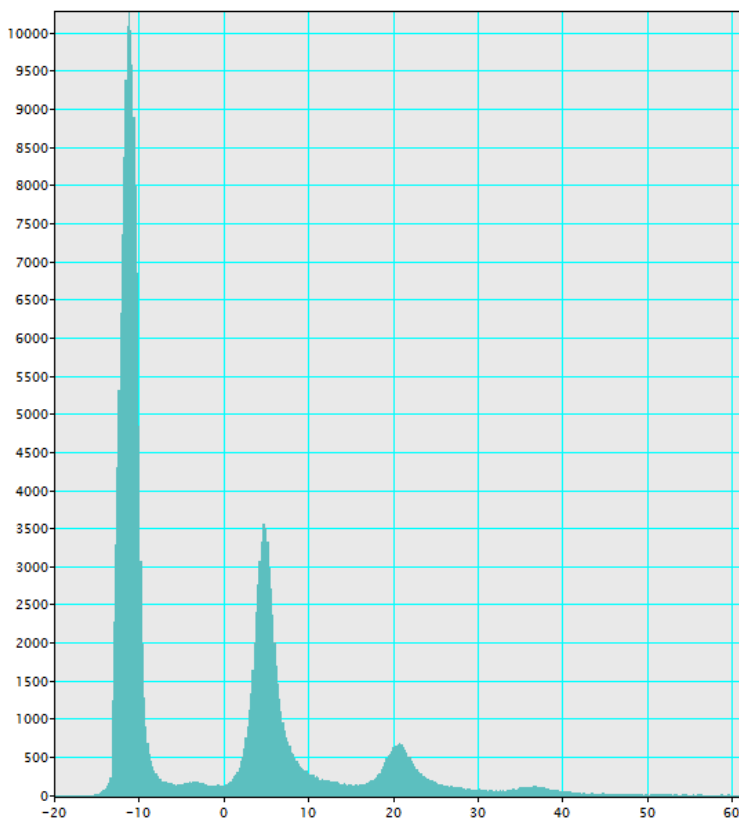
Figure 4.15: Electron Energy Loss Spectroscopy for **Fig. 4.14**.

For case 3 there were some problems achieving good pictures, arguably due to the samples being thinner causing lack of contrast. **Fig. 4.16** was used for statistics on area and density, while **Fig. 4.17** was used for measuring length of the precipitates. **Fig. 4.18** shows the EELS for **Fig. 4.16**.
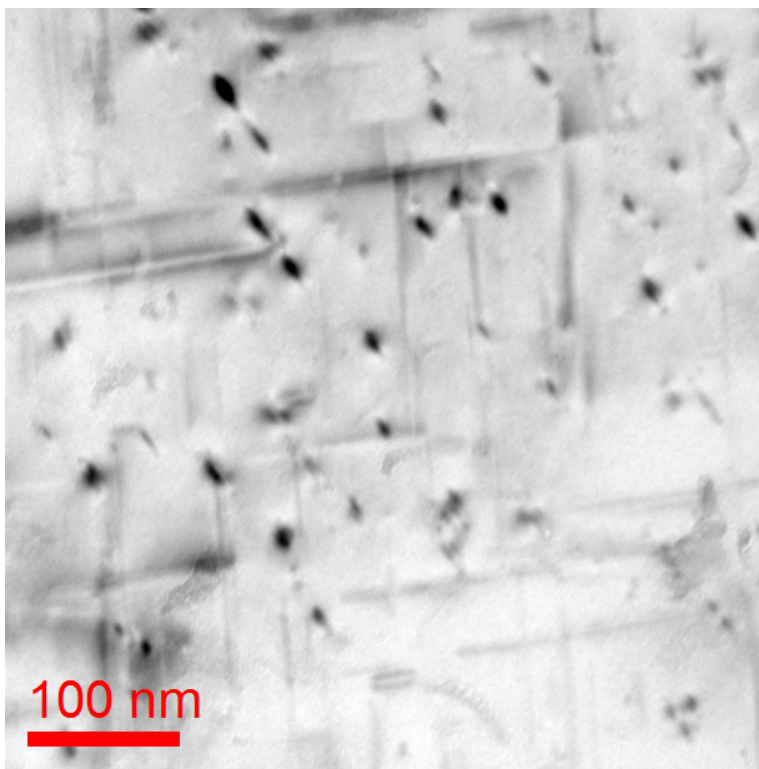
Figure 4.16: The image used for measuring the area and the particle area and density.
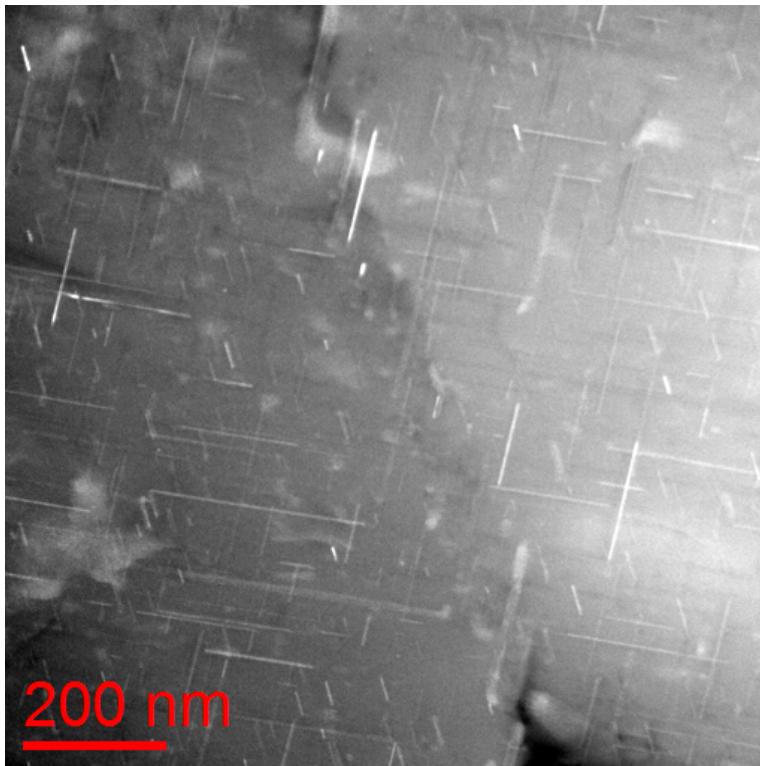
Figure 4.17: The image used for measuring the particle length.
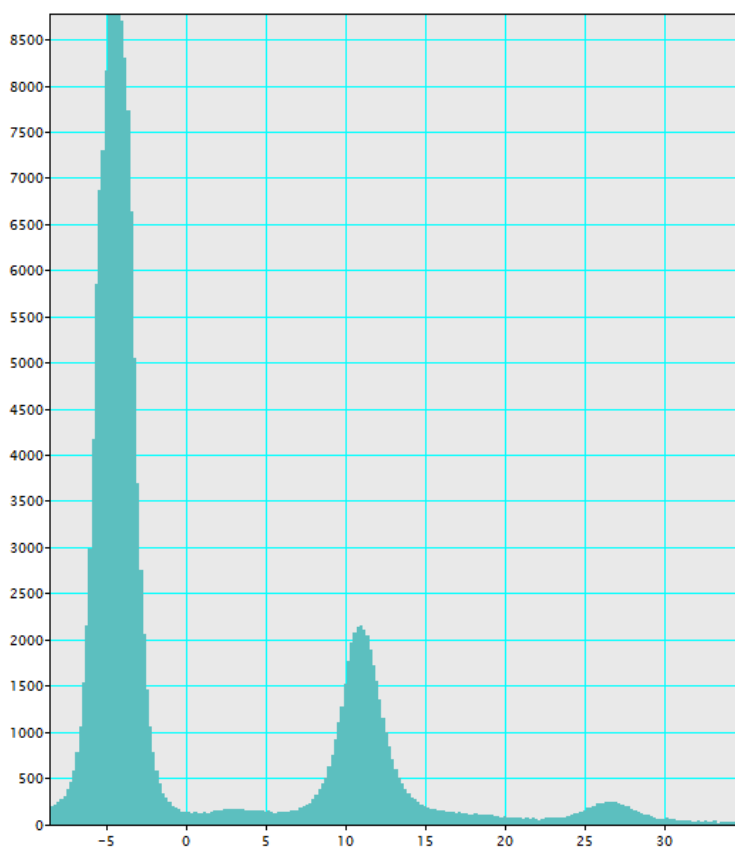
Figure 4.18: Electron Energy Loss Spectroscopy for **Fig. 4.16**.

4.4 TEM pictures and particle statistics

For analysing the EELS and for all the measuring done on the pictures, the program Gatan Micrograph was used. Finding the area of the particles was done by measuring the longest diameter and the diameter normal to the first one as shown in **Fig. 4.19**, the area is then found by multiplying L1 and L2. **Fig. 4.20** shows how it would look like, although the lines seen in the image are not the actual measurements, they give a graph showing light intensity, which was used to find the diameter across more accurately.
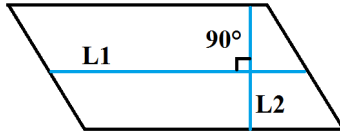
Figure 4.19: Illustration of how area measurements were done.
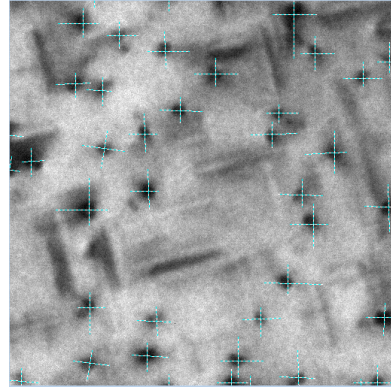
Figure 4.20: Area measurements in T6.

Another interesting statistic that was not found, was the simultaneously measurement of length and width of horizontal needle particles. **Fig. 4.22** shows in the red circle a particle in the z direction and in the blue box a particle in the X or Y direction like the ones that were used to find the length distributions. The thick black lines along the particle are stress fields, and the thickness of these lines vary a lot making it difficult finding a reliable and consistent width of the particles in the X and Y directions, so all the diameters and areas are found from measuring the cut of particles in the Z direction.
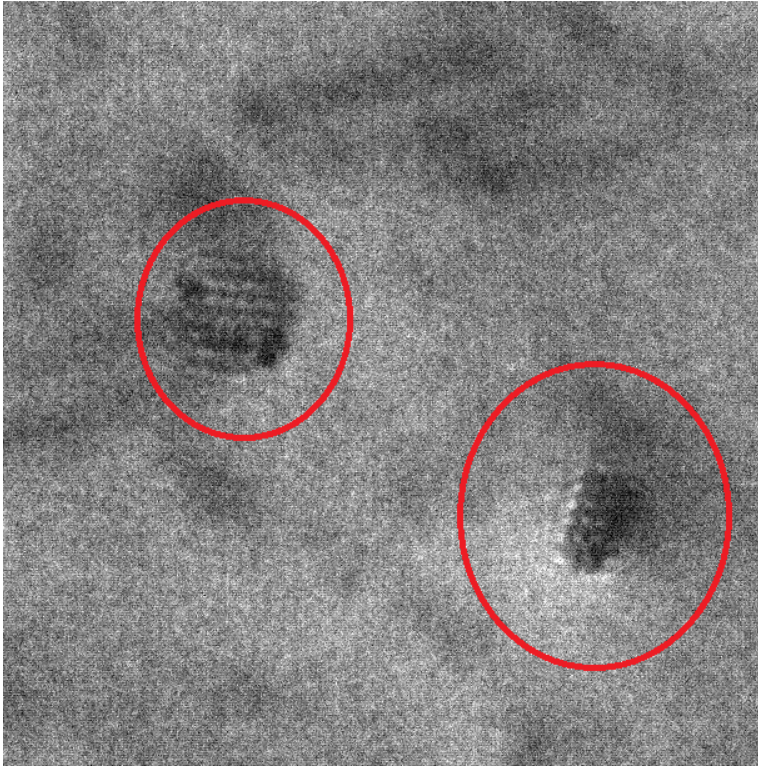
Figure 4.21: Close look on high resolution particles.
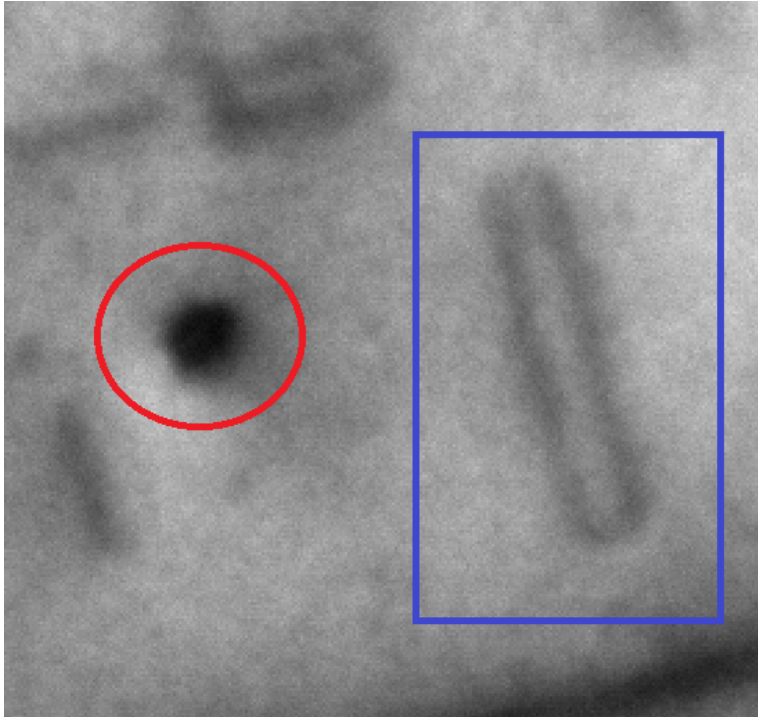
Figure 4.22: A particle in Z direction and a particle in X or Y direction.

The mean free path (λ) for this alloy was found to be $80\,\mathrm{nm}$ from experts in the field at the faculty. Some of the numbers found from the analysis are listed in **Table 4.6**.

Table 4.6: Some statistics from TEM image analysis.

Case	Case 1, T6	Case 2	Case 3
Average Length [nm]	20.4	201	144
Average Area [nm^2]	16.4	43	54.3
Average Diametre [nm]	3.94	6.41	7.2
Area of Photo used for density [nm^2]	1.79E+05	2.01E+06	6.89E+05
Mean Free Path (λ) [nm]	80	80	80
$ln(I_t/I_0)$	0.65	0.65	0.36
Local thickness [nm]	52	52	28.8
Particle density [nm^{-3}]	1.16E-04	1.58E-06	3.30E-06
$Volume_P/Volume$ [%]	3.87	1.36	2.58

Only looking at the data in **Table 4.6**, it is easy to see that the over aging has had a huge impact on the precipitates. A long precipitate will block dislocations from more slip planes, therefore longer precipitates are preferable. They need to be non shearable to stop the dislocations, and the diameter limit between shearable and non shearable has been found earlier to be close to $3\,\mathrm{nm}$ [21]. Case 2, which was over aged at $185\,^\circ\mathrm{C}$, has

Table 4.7: Relation between the particle densities.

Density relations	
T6 / Case2	73.22
T6 / Case3	35.02
Case 3 / Case 2	2.09

an average length at $200\,\mathrm{nm}$, which is 10x as long as the average length in T6. Case 3 also experienced a lot of growth, growing the average length to $144\,\mathrm{nm}$. The average area for case 2 and 3 are $43\,\mathrm{nm}$ and $54.3\,\mathrm{nm}$ respectively, this is a lot higher than the average area for T6, which was found to be $16.4\,\mathrm{nm}$. However the reason the material is not as strong, can be seen from the particle density. **Table. 4.7** shows the relation between the densities of the different cases. The particle density is $\approx$ 70x higher at T6 than for case 2 and 35x higher for case 3. The volume has been adjusted by using **Eq.** (2.2) when finding the density and when finding $Volume_P/Volume$, where $Volume_P$ is the average cross section area times average length times number of particles, and $Volume$ is the volume of the local sample spot.

However only looking at the average of the measurements can be somewhat misleading, therefore the distributions of length and area has been plotted below. The distribution in **Fig. 4.23** shows a very condensed grouping with close to 90% of the precipitates being between 10-30 nm. This is not the case for case 2 as it is much more scattered as seen in **Fig. 4.24**. It seems like the the precipitates would all grow at different rates, most would grow to have a length somewhere between 40-180 nm which is a huge gap, but still some few where found to be at different lengths from $180\,\mathrm{nm}$ all the way up to $518\,\mathrm{nm}$. For case 3 as seen in **Fig. 4.25** it seems that there is a preferred length between 40-240 nm with less particles of extreme lengths above $240\,\mathrm{nm}$.
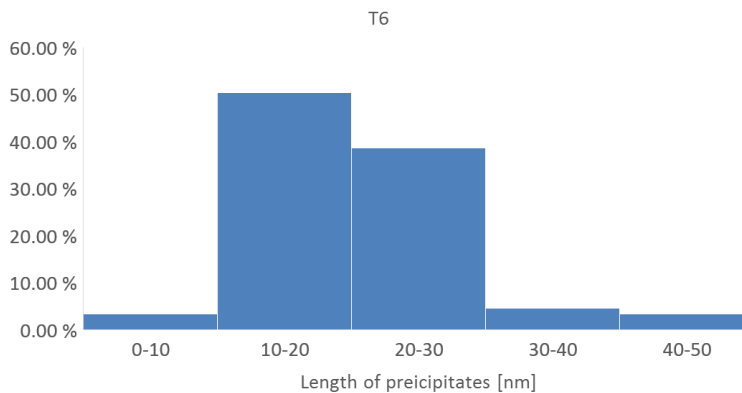
Figure 4.23: The length distribution in T6.
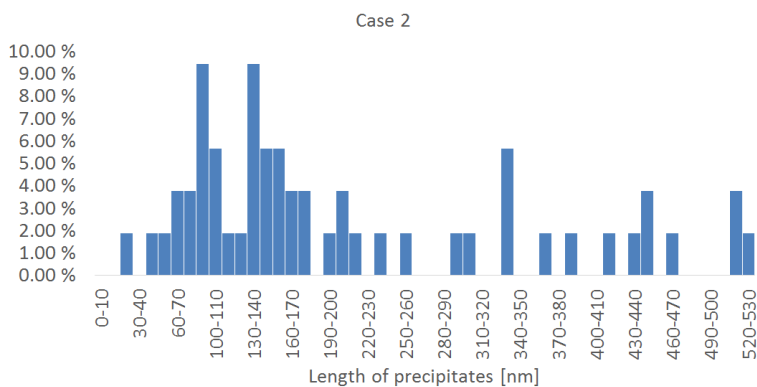
Figure 4.24: The length distribution in Case 2.
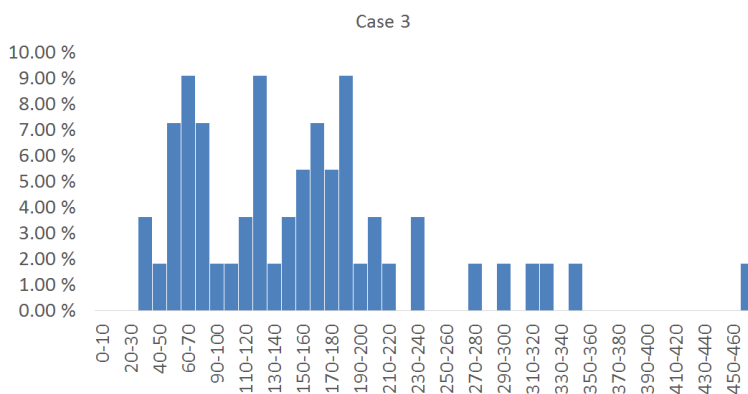
Figure 4.25: The length distribution in Case 3.

The per cent distribution does not really show the difference between T6, case 2 and case 3 since it does not consider the particle density. Therefore **Fig. 4.26**, **Fig. 4.27** and **Fig. 4.28** has been plotted where the distribution is numbers of particles divided by the corrected volume discussed in theory.
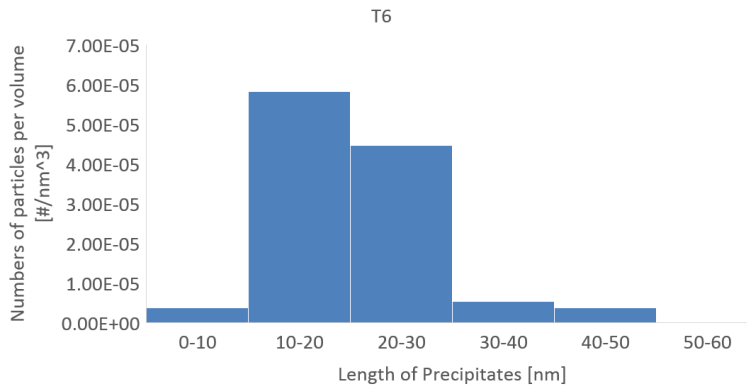
Figure 4.26: The length distribution in T6. Particles per volume.
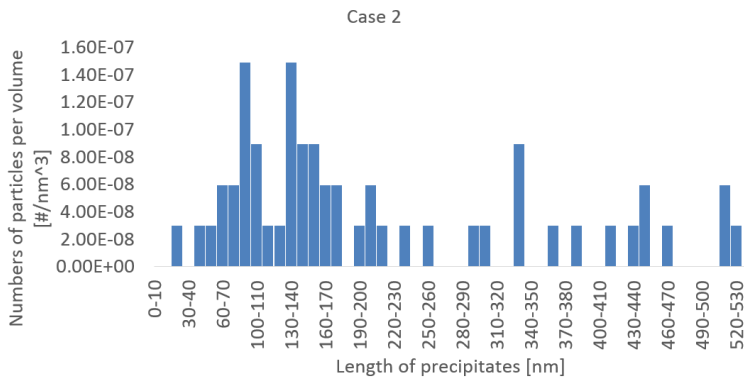
Figure 4.27: The length distribution in Case 2. Particles per volume.
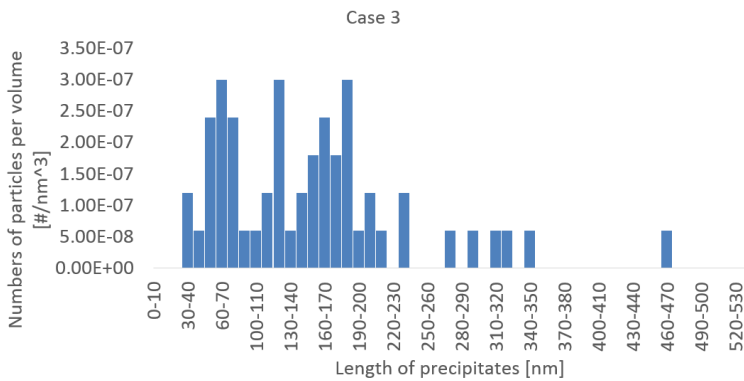
Figure 4.28: The length distribution in Case 3. Particles per volume.

The area distribution for T6 shown in **Fig. 4.29** is very centered around 5-30 nm^2, there are very few particles outside of that range. For case 2 **Fig. 4.30** shows an increase in the span that holds the clear majority of the particle areas, the distribution seems to flatten out a lot more. Finally for case 3 as seen in **Fig. 4.31**, it is observed that there is a higher concentration of particles with higher area and a less even distribution.
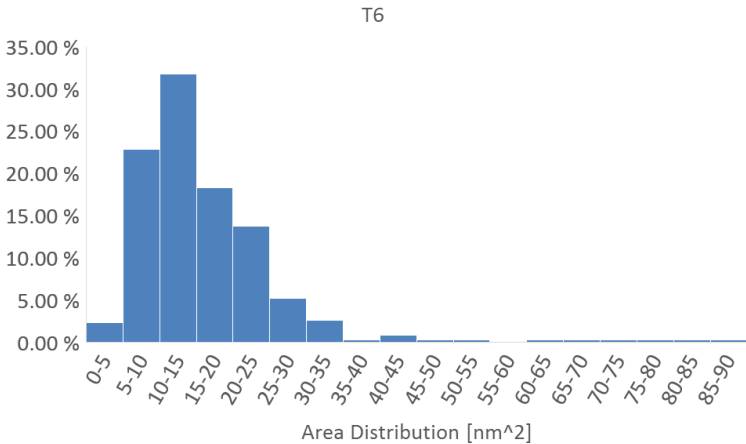
Figure 4.29: The cross section area distribution in T6.
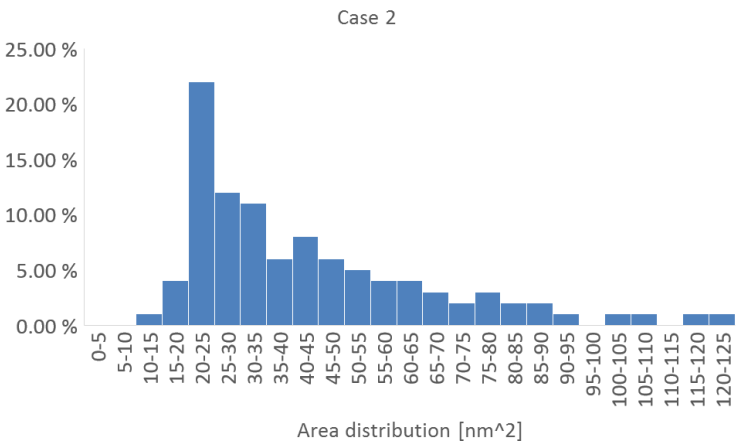
Figure 4.30: The cross section area distribution in Case 2.
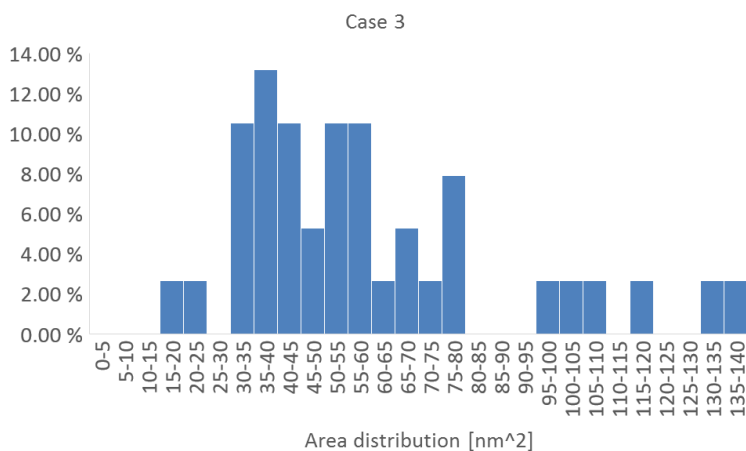
Figure 4.31: The cross section area distribution in Case 3.

Same as with the length distribution, an area distribution with particles per volume is shown below for T6, case 2 and case 3 in **Fig. 4.32**, **Fig. 4.33** and **Fig. 4.34** respectively.
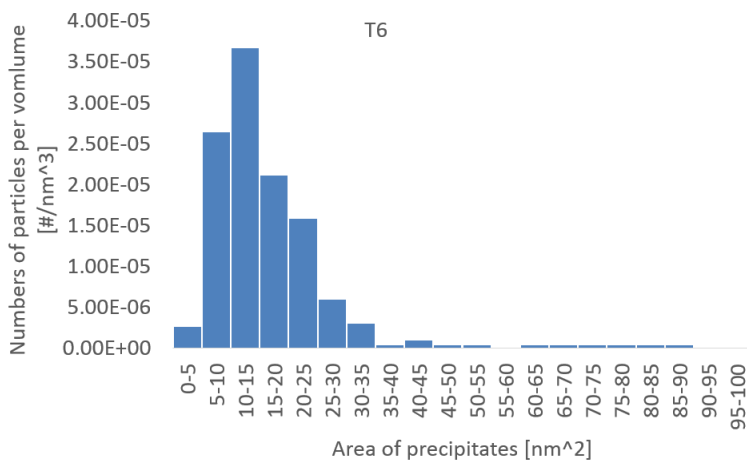
Figure 4.32: The cross section area distribution in T6. Particles per volume.
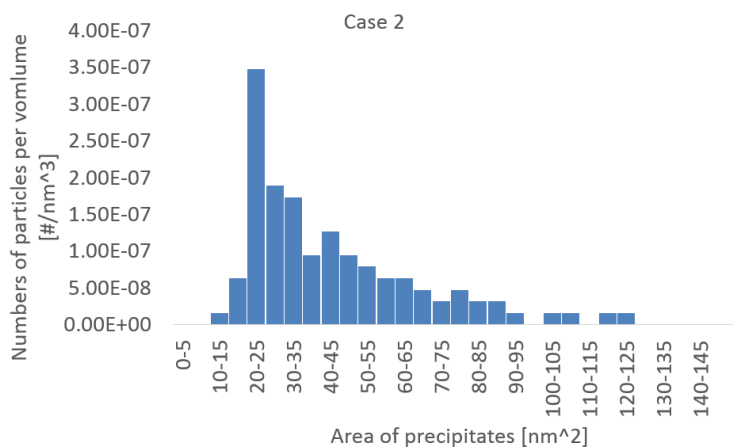
Figure 4.33: The cross section area distribution in Case 2. Particles per volume.
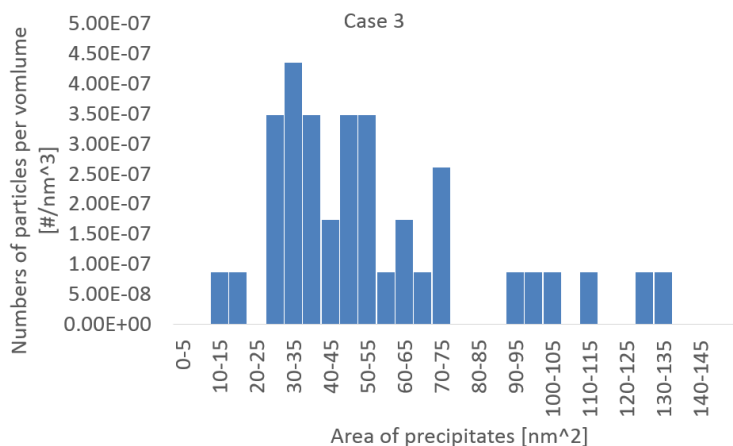
Figure 4.34: The cross section area distribution in Case 3. Partiicles per volume.

Chapter 5

Discussion

This chapter discusses all the results found and will connect the experimental results with the presented earlier.

5.1 Hardening curve

The reason the hardness falls after T6 even though the precipitates gets longer and assumed all non-shearable is the decrease in the particle density. T6 has a high particle density, and **Fig. 5.1** shows a distribution of non-shearable/shearable particles based on a critical shearable area, and as seen most particles are non-shearable or close to non-shearable. The shearable particles in T6 are so close to non-shearable that they are still very strong pinning points for the dislocations. The shearable/non-shearable criterion was set to $3\,\text{nm}$ diameter which will give an area of $9\,\text{nm}^2$ assuming equal diameters, but since that is not the case $10\text{-}12\,\text{nm}^2$ is set as a danger zone where the precipitates might be slightly shearable. The higher temperature, in this case $200\,^\circ\text{C}$, causes a faster diffusion of Mg and Si making the big precipitates grow and the smaller precipitates to dissolve faster. However, it is not obvious whether the two cases are equal when it comes to the state of precipitates by just looking at the hardness curves. Therefore all the distributions are discussed later in the report.
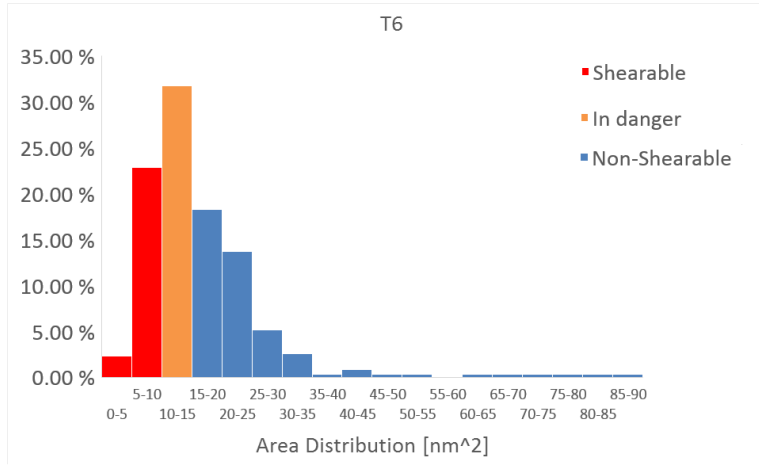
Figure 5.1: Cross section area distribution for T6. Red columns are shearable particles, orange is presumed a mix of shearable and non-shearable, and blue are presumed non-shearable based on the size of the cross section area.

5.2 Tensile tests

All the E-modules are between 70-73 GPa except for sample 10-12 which are the only solutionized samples. The values are too low for aluminium alloys and that can be a result of the yield strength being as low, not giving enough values to cover a straight section. All the E-modules are found by $\Delta Stress/\Delta Strain$ for a section centred on the middle of the elastic part on the stress/strain-curve. However since the elastic zone is so small, a lot less values was used, causing any early deviations in the very beginning of the test to have an impact on the E-module.

The phenomenon observed for samples 10-12 in **Fig. 5.2** causing the serrated nominal stress-strain curve is called the Portevin-Le Chatelier effect (PLC). This has to do with the dynamic strain ageing (DSA), which is the competition between solutes pinning the dislocation and the dislocations breaking free. Because DSA is due to the Mg and Si in solid solution, it is only observed in samples 10-12. [22]
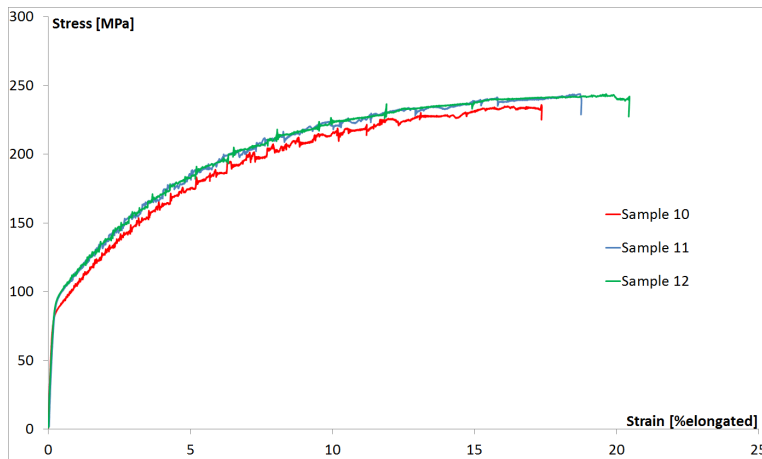
Figure 5.2: Nominal stress strain for sample 10-12, the samples only solutionized.

Samples 10-12 work hardens a lot through the test. T6 however, experiences almost no work hardening at all, the nominal curve is almost completely flat, while the true curve has some inclination. The over aged cases 2 and 3 has a work hardening in-between the two other cases. All this can be observed in **Fig. 5.3**. A curve for commercially pure aluminium AA 1050 (orange) has been added to emphasize the particle and solid solution contribution to the work hardening. The difference between the solutionized samples and the AA 1050 are the solid solution Mg and Si in the solutionized samples, meaning the difference in work hardening between W and AA 1050 must be the hardening contribution from the Mg and Si [23]. Initially the work hardening rate is higher in T6 than in the AA 1050, the reason for this could be the formation of dislocation loops around the precipitates in the very beginning of the stretching. T6 has a lot of non-shearable particles as seen **Fig. 5.1** and a high density of precipitates which makes it possible for a lot of dislocation loops to be formed. After the extra high work hardening rate, annealing of the dislocation loops starts happening and the effect is lost. Case 2 and 3 probably experience the same effect, especially since they are presumed to only contain non-shearable particles. The list below sums up this paragraph.

- More Mg and Si in solid solution increase the $d\sigma/d\varepsilon$.

- Particles yield geometrical necessary dislocations and increased $d\sigma/d\varepsilon$ for small strains.

- Mix of obstacles will give a flat initial curve $d\sigma/d\varepsilon = 0$.
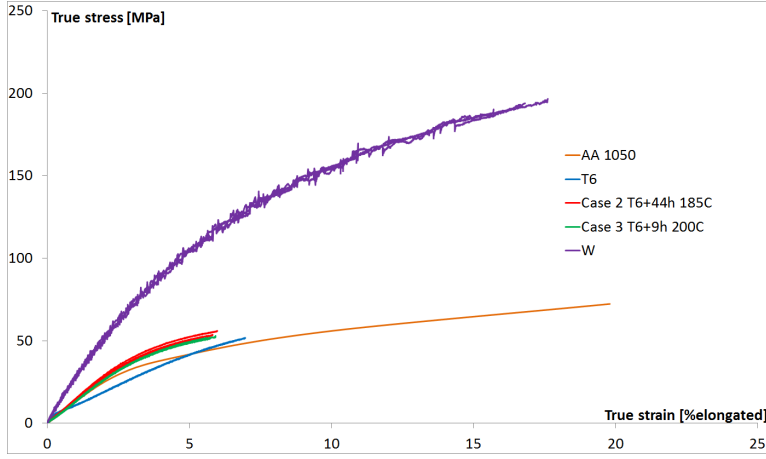
Figure 5.3: Work hardening contribution

One possible explanation for why the T6 curve is so flat is outlined below. The obstacles present inside the material are n_p and n_d, where n_p is the number of precipitates and n_d is the number of dislocations per glide plane area, and then the average distance between any dislocation pinning point in the glide plane, either precipitates or dislocations, are: [24]

$$l = \frac{1}{\sqrt{n}} = \frac{1}{\sqrt{n_p + n_d}} \tag{5.1}$$

The contribution of only the precipitates present is τ_P, and is given by:

$$\tau_P = \frac{k * G * b}{l_P} = k_P * G * b * \sqrt{n_P} \tag{5.2}$$

where G is the shear modulus, b the magnitude of the Burgers vector, k is some constant and l_P is the distance between the precipitates. The contribution of the dislocations is:

$$\tau_d = k_d * G * b * \sqrt{n_d} \tag{5.3}$$

Assuming no difference between the obstacles, the contribution from any obstacle is shown in **Eq. 5.4**

$$\tau = \alpha * G * b * \sqrt{n} \tag{5.4}$$

k is a constant. But now it is observed that if **Eq.** (5.1) is flipped, squared and multiplied with $(G * b)^2$ as seen in **Eq.** (5.5), it will yield **Eq.** (5.6). Now it is assumed $\alpha \approx K_d \approx K$.

$$\left(\frac{1}{\sqrt{n}}\right)^{-2} * (G*b)^2 = \left(\frac{1}{\sqrt{n_P + n_d}}\right)^{-2} * (G*b)^2 = n*(Gb)^2 = (n_P + n_d)*(Gb)^2 \quad (5.5)$$

$$\tau^2 = \tau_P^2 + \tau_d^2 \quad (5.6)$$

Finally what is wanted to know is the work hardening, or how the contribution changes $\frac{d\tau}{d\gamma}$.

$$2 * \tau \frac{d\tau}{d\gamma} = 2 * \tau_d * \frac{d\tau_d}{d\gamma} + 2 * \tau_P * \frac{d\tau_p}{d\gamma} \quad (5.7)$$

$\frac{d\tau_P}{d\gamma}$ is of course 0, as the number of precipitates doesn't change. Then the equation becomes:

$$\frac{d\tau}{d\gamma} = \frac{\tau_d}{\tau} * \frac{d\tau_d}{d\gamma} \quad (5.8)$$

And since $\tau_P \gg \tau_d$, it means $\tau \gg \tau_d$ which gives $\frac{\tau_d}{\tau} \ll 1$. Which is why the curve is so flat initially, when there are still few dislocations at low strains [24].

5.3 Precipitate distribution

Fig. 5.4 is a plot of the two diameters measured (see **Fig. 4.19** for each cross section area plotted against each other for all the cases. It shows a clear centering around $f(x) = x$ which means they are close to being a perfect square. A difference in the scattering could indicate a different types of particles present in the sample due to their different atomic structures. Case 2 and to some degree case 3, seems to be scattered more away from the $f(x) = x$ line, but the resolution in the pictures taken are not good enough to find any particle distribution from this.
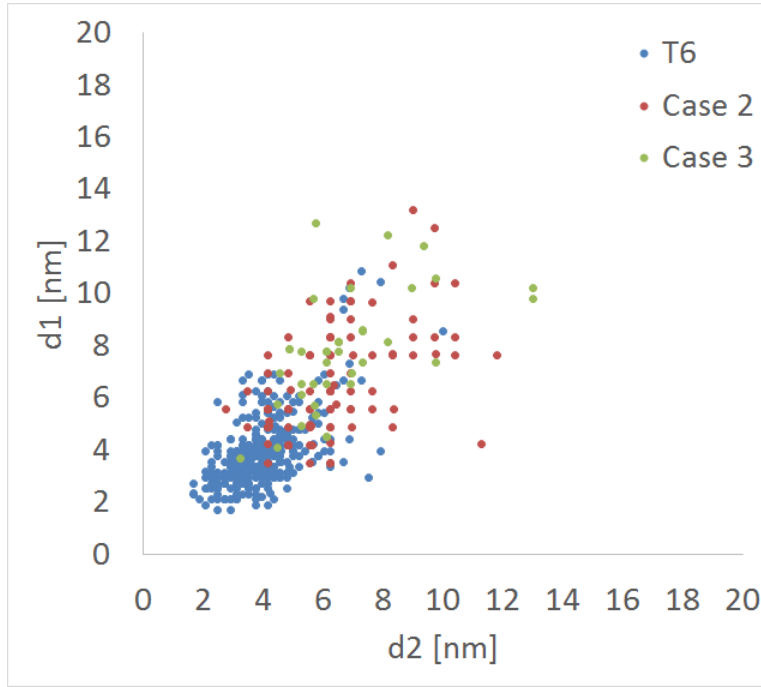
Figure 5.4: The two cross section diameters measured for each particle plotted against each other.

Fig. **5.5** shows the length distribution and **Fig. 5.6** shows the area distribution of all the three cases in the same graphs. Case 3 has a lower average length, but a higher average cross section area and a twice as high particle density compared to case 2. This could mean case 3 loses its strength faster not only because of the higher temperature giving a faster diffusion speed, but because at higher temperature it prefers growing in width. Increasing the area is not favorable after the precipitates are non-shearable, all growth should optimally be in the length direction to intercept more slip planes, this can explain why case 3 even with almost twice as high particle density still has the same hardness.
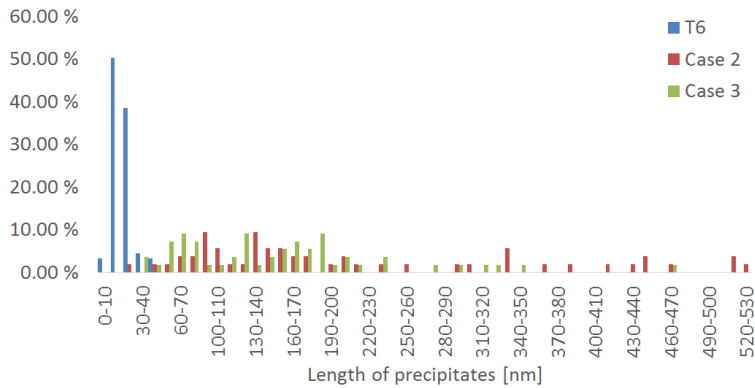
Figure 5.5: The length distribution for all cases.
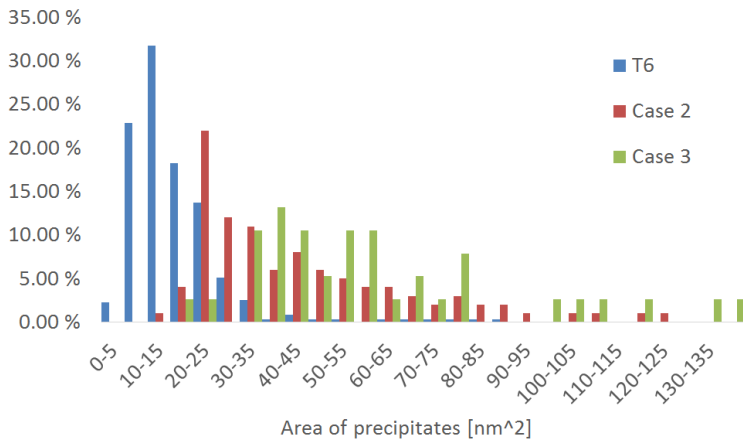
Figure 5.6: The area distribution for all cases.

The percent distribution does however not take into consideration the particle density, so **Fig. 5.7** and **Fig. 5.8** shows the length distribution and area distribution respectively as particles per corrected volume for case 2 and case 3. This helps show the difference in distributions and density as discussed above. Similar graphs containing T6 as well can be seen in the appendix in **Fig. 7.1** and **Fig. 7.2**, but due to the particle density in T6 being remarkably higher than the particle density for case 2 and case 3 the graphs shows almost nothing more than the distributions of T6.

Fig. 5.9 is a graph showing the average area plotted against the average length of the three cases. This is not enough data for any good trend line or statistical analysis, however from what has been discussed as possible trends it can seem that after T6, materials over aged at higher temperatures will have higher and shorter trend lines as a result of higher temperature gives bigger area and shorter lengths.

A reason for the difference in length and cross section area between case 2 and 3 could be they have different particle distributions. β' particles grow longer than β" [25], this implies that case 3 contains more β" and case 2 contains more β', or even possibly some other over aged precipitates like B' etc. Assuming this to be true, it means at higher temperatures the precipitates prefers to grow as β", but at lower temperatures for the precipitates to keep growing they change to β' particles. This is mostly speculations as it was not possible to obtain actual particle distributions from the results.
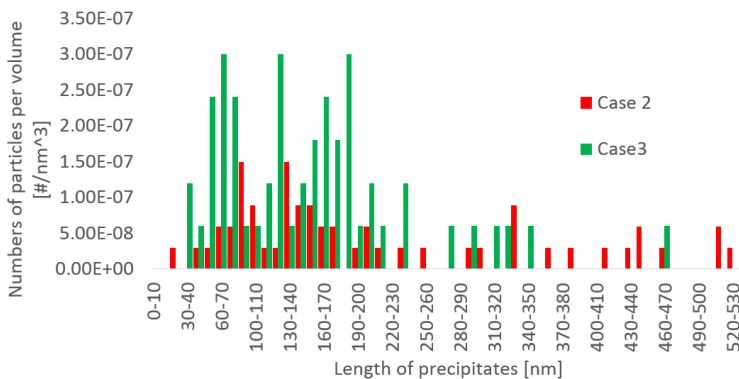
Figure 5.7: Length distribution for case 2 and 3. Particles per volume.
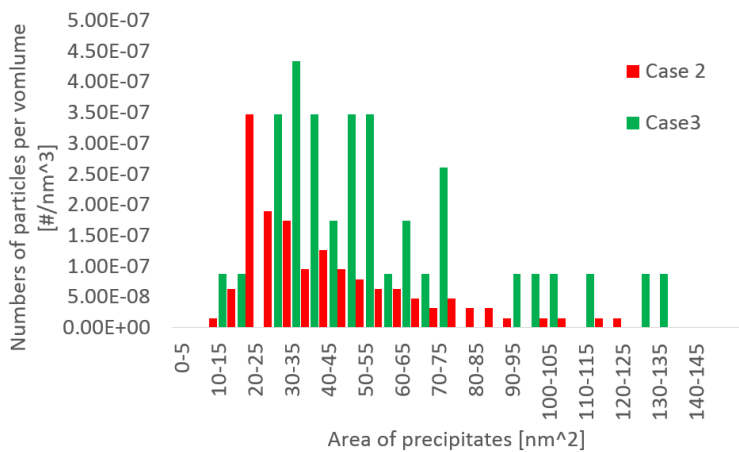
Figure 5.8: Length distribution for case 2 and 3. Particles per volume.

Figure 5.9: The average area plotted against the average length of the three cases.

Even with the highest resolution achieved on the microscope used for this thesis as shown in **Fig. 4.21**, it still was not good enough for finding an actual particle distribution, so it is not known how many particles are β", β' or any other particles that may appear in the over aging. The reason is the pictures not being sharp enough to d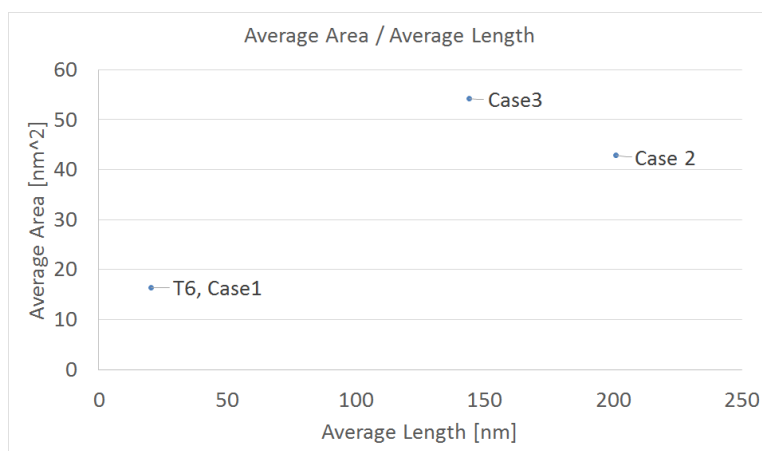etermine the angle of the corners in the cross section precipitates. A higher resolution microscope would solve this problem, or in theory it could be possible to use ASTAR, which is an automatic mapping tool for TEM, that can map different orientations and phases, and it can also do crystallographic indexing. It can therefore be used on a smaller area and find the different phases representing the different types of precipitates and automatically finding a particle distribution. This has however not been done like this, and it is uncertain if it would be accurate enough to work.

5.4 Sources of error

All the hardness tests are done on an old machine where setting the lines and making sure the lines hit at the right angle are done manually, this can make up for some error and the best way to negate this is to do several tests each time. The extruded plate itself has a lot of curves, bends and scratches showing signs of some ruff handling over the years since it was extruded. To remove errors from the surface being scratched and bent, the samples were grinded till the surface was smooth and flat.

The tensile tests did sometimes experience the actual fracture happen outside the range of the extensometer, but running three parallels is a way to help negate the problem. There were some problems with the E-module for sample 10-12 for the only solutionized case. Other possible solutions to the low E-module might be the samples were from a part of the extruded plate containing some curvature, or they might not have been fastened straight.

Fig. 4.13 shows a precipitation free zone along the grain boundary at T6. Precipitation free zones weakens the material as the dislocations can move more unhindered, and is therefore unwanted in the material. The precipitation free zones may be formed as a result

of the vacancies being absorbed by grain boundaries, hindering the nucleation[26][27]. A long time spent between finished solutionizing and quenching will result in larger precipitation free zones. Large precipitation free zones would be a source of error, but in this case it is assumed that the zones are small as in **Fig. 4.13** for all the cases as the samples were all quenched directly after solutionizing.

The biggest source of error lies within finding the statistics by measuring the particles in the TEM-pictures. Due to the lack of experience handling the TEM there is a difference in quality in the pictures. The stress fields would make it hard to see the exact length of the particles, possibly missing the exact length up to $\approx 5\,\mathrm{nm}$. When measuring the area of the cross section particles the area was found by multiplying L1 and L2 that were found as illustrated in **Fig. 4.19**, however it was difficult getting the pictures sharp enough to see the shape clear enough, resulting in some error. The black colour representing the cross section particles were also often fading to some degree, making it personal judgement call telling their size. This rarely made out to be more than 1-1.5 nm for L1 and L2, but since the diameters are so small as shown in tables above this might be the statistic most affected by personal judgements and therefore the most susceptible to error. In **Fig. 5.1** showing the area distribution of T6 with color codes showing the distribution of non-shearable/shearable it is observed that a small measurement error of about 1-1.5 nm in the diameter can skew the distribution considerably. T6 had the best pictures and the most precipitates in the good pictures making it the case with the most statistics, Case 2 also had some good pictures giving a lot of statistics. There was some trouble achieving good results for case 3, there was some good pictures finding the length distribution, but the area distribution for case 3 is the statistic with the least amount of measurements, and will yield some source of error.

Finding the particle density was done by using Electron Energy Loss Spectroscopy (EELS), which is considered to be a very rough approximation when used to find the local thickness of a sample. The mean free path (λ) is dependent on a lot of factors, like the composition and crystal structure of the material, yet only an estimate was advised to be used by experienced professors at the department.

Chapter 6

Conclusion

This thesis contains some of the experimental data needed for the development of geometry dependant models. It contains statistical distributions of length and area of precipitates in three cases. The first case is at peak hardness called T6, as this is the industry relevant case. The other two cases are $\approx 70\%$ of the peak hardness achieved by over aging at $185\,^\circ\text{C}$ and $200\,^\circ\text{C}$ after T6. From the tensile tests and the distributions a few conclusions has been made, as seen in the list below.

- Increased initial work hardening rate in over aged conditions as compared to T6.

- During over aging the smaller precipitates dissolve to feed the growth of the bigger precipitates, this causes a lower density of particles resulting in a longer distance between dislocation pinning points. The particle density at T6 is considerably higher than for both the over aged materials.

- Aging at $200\,^\circ\text{C}$ resulted in relatively thicker needles as compared to at $185\,^\circ\text{C}$.

- Aging at $200\,^\circ\text{C}$ resulted in some very large particles, which consumes solute at the expense of efficient hardening.

- The difference in length and cross section area for the over aged materials can be explained by the material over aged $185\,^\circ\text{C}$ containing more β', and $185\,^\circ\text{C}$ containing more β'', as β' particles has been found in other reports to grow longer than β''. This can not be proven in this report due to the lack of a particle distribution graph.

Chapter 7

Further work

The models needs a lot of experimental data, and the results from this work is only a small fraction of it. Therefore the most obvious plan for further work would be to keep on getting experimental data in big amounts. Finding length and cross section area distributions for different tempers and alloys, and more statistics for the precipitate length plotted against cross section area seeing if this could be used to find a transition between the different particles. Another step is seeing if using the ASTAR could work to automatically get a distribution of the different particles, as this would lower the time to gather statistics immensely. Any work done with the intent of studying the mechanics of the needle shaped precipitates, for example by studying how they transform from β" to the other over aged precipitates would help understand the precipitates better and could help with modeling.

Bibliography

[1] Ryen Ø. Work Hardening and Mechanical Anisotropy of Aluminium Sheets and Pro-files [Doctor Thesis]; 2003.

[2] Myhr OR, Grong Ø. Modelling of non-isothermal transformations in alloys containing a particle distribution [Journal Article]. Acta Materialia. 2000;48(7):1605–1615. Available from: `http://www.sciencedirect.com/science/article/pii/S1359645499004358`.

[3] Holmedal B, Osmundsen E, Du Q. Precipitation of Non-Spherical Particles in Aluminum Alloys Part I: Generalization of the Kampmann–Wagner Numerical Model [Journal Article]. Metallurgical and Materials Transactions A. 2016;47(1):581–588. Available from: `http://dx.doi.org/10.1007/s11661-015-3197-5`.

[4] Du Q, Holmedal B, Friis J, Marioara CD. Precipitation of Non-spherical Particles in Aluminum Alloys Part II: Numerical Simulation and Experimental Characterization During Aging Treatment of an Al-Mg-Si Alloy [Journal Article]. Metallurgical and Materials Transactions A. 2016;47(1):589–599. Available from: `http://dx.doi.org/10.1007/s11661-015-3196-6`.

[5] Earnshaw A, Greenwood N. In: 7 - Aluminium, Gallium, Indium and Thallium. Oxford: Butterworth-Heinemann; 1997. p. 216–267. Available from: `http://www.sciencedirect.com/science/article/pii/B9780750633659500134`.

[6] Takeda M, Ohkubo F, Shirai T, Fukui K. Stability of metastable phases and microstructures in the ageing process of Al–Mg–Si ternary alloys [Journal Article]. Journal of Materials Science. 1998;33(9):2385–2390. Available from: `http://dx.doi.org/10.1023/A:1004355824857`.

[7] Marioara CD, Andersen SJ, Jansen J, Zandbergen HW. Atomic model for GP-zones in a 6082 Al–Mg–Si system [Journal Article]. Acta Materialia. 2001;49(2):321–328. Available from: `http://www.sciencedirect.com/science/article/pii/S1359645400003025`.

[8] Hasting HS, Frøseth AG, Andersen SJ, Vissers R, Walmsley JC, Marioara CD, et al. Composition of β" precipitates in Al–Mg–Si alloys by atom probe tomography and first principles calculations [Journal Article]. Journal of Applied Physics. 2009;106(12):123527. Available from: http://scitation.aip.org/content/aip/journal/jap/106/12/10.1063/1.3269714.

[9] Andersen SJ, Zandbergen HW, Jansen J, Træholt C, Tundal U, Reiso O. The crystal structure of the β" phase in Al–Mg–Si alloys [Journal Article]. Acta Materialia. 1998;46(9):3283–3298. Available from: http://www.sciencedirect.com/science/article/pii/S135964549700493X.

[10] Edwards GA, Stiller K, Dunlop GL, Couper MJ. The precipitation sequence in Al–Mg–Si alloys [Journal Article]. Acta Materialia. 1998;46(11):3893–3904. Available from: http://www.sciencedirect.com/science/article/pii/S1359645498000597.

[11] Ninive PH, Løvvik OM, Strandlie A. Density Functional Study of the β" Phase in Al-Mg-Si Alloys [Journal Article]. Metallurgical and Materials Transactions A. 2014;45(6):2916–2924. Available from: http://dx.doi.org/10.1007/s11661-014-2214-4.

[12] Ninive PH, Strandlie A, Gulbrandsen-Dahl S, Lefebvre W, Marioara CD, Andersen SJ, et al. Detailed atomistic insight into the β" phase in Al–Mg–Si alloys [Journal Article]. Acta Materialia. 2014;69:126–134. Available from: http://www.sciencedirect.com/science/article/pii/S1359645414000731.

[13] Bjerkaas H. Characterisation and Plasticity in Extruded Al-Mg-Si Profiles engaging In-situ EBSD [Doctor Thesis]; 2007.

[14] Ryen Ø, Holmedal B, Marthinsen K, Furu T. Precipitation, strength and work hardening of age hardened aluminium alloys [Journal Article]. IOP Conference Series: Materials Science and Engineering. 2015;89(1):012013. Available from: http://stacks.iop.org/1757-899X/89/i=1/a=012013.

[15] Holmedal B. Strength contributions from precipitates [Journal Article]. Philosophical Magazine Letters. 2015;95(12):594–601. Available from: http://dx.doi.org/10.1080/09500839.2015.1125029.

[16] Du Q, Holmedal B, Friis J, Marioara C. Precipitation of Non-spherical Particles in Aluminum Alloys Part II: Numerical Simulation and Experimental Characterization During Aging Treatment of an Al-Mg-Si Alloy [Journal Article]. Metallurgical and Materials Transactions A. 2015;p. 1–11. Available from: http://dx.doi.org/10.1007/s11661-015-3196-6.

[17] Holmedal B, Osmundsen E, Du Q. Precipitation of Non-Spherical Particles in Aluminum Alloys Part I: Generalization of the Kampmann–Wagner Numerical Model [Journal Article]. Metallurgical and Materials Transactions A. 2015;p. 1–8. Available from: http://dx.doi.org/10.1007/s11661-015-3197-5.

[18] Dieter GE. Mechanical Metallurgy; 1988.

[19] Solberg JK, Hansen V. Innføring I Transmisjon Elektronmikroskpi;.

[20] Egerton RF. 5. In: TEM Applications of EELS. Springer US; 2011. p. 293–397. Available from: `http://dx.doi.org/10.1007/978-1-4419-9583-4_5`.

[21] Poole * WJ, Wang X, Lloyd DJ, Embury JD. The shearable–non-shearable transition in Al–Mg–Si–Cu precipitation hardening alloys: implications on the distribution of slip, work hardening and fracture [Journal Article]. Philosophical Magazine. 2005;85(26-27):3113–3135. Available from: `http://dx.doi.org/10.1080/14786430500154935`.

[22] Dierke H, Krawehl F, Graff S, Forest S, Šachl J, Neuhäuser H. Portevin–LeChatelier effect in Al–Mg alloys: Influence of obstacles – experiments and modelling [Journal Article]. Computational Materials Science. 2007;39(1):106–112. Available from: `http://www.sciencedirect.com/science/article/pii/S092702560600139X`.

[23] Ryen Ø, Holmedal B, Nijs O, Nes E, Sjölander E, Ekström HE. Strengthening mechanisms in solid solution aluminum alloys [Journal Article]. Metallurgical and Materials Transactions A. 2006;37(6):1999–2006. Available from: `http://dx.doi.org/10.1007/s11661-006-0142-7`.

[24] Cheng LM, Poole WJ, Embury JD, Lloyd DJ. The influence of precipitation on the work-hardening behavior of the aluminum alloys AA6111 and AA7030 [Journal Article]. Metallurgical and Materials Transactions A. 2003;34(11):2473–2481. Available from: `http://dx.doi.org/10.1007/s11661-003-0007-2`.

[25] Vissers R, van Huis MA, Jansen J, Zandbergen HW, Marioara CD, Andersen SJ. The crystal structure of the β' phase in Al–Mg–Si alloys [Journal Article]. Acta Materialia. 2007;55(11):3815–3823. Available from: `http://www.sciencedirect.com/science/article/pii/S1359645407001796`.

[26] Marioara CD, Andersen SJ, Jansen J, Zandbergen HW. The influence of temperature and storage time at RT on nucleation of the β'' phase in a 6082 Al–Mg–Si alloy [Journal Article]. Acta Materialia. 2003;51(3):789–796. Available from: `http://www.sciencedirect.com/science/article/pii/S1359645402004706`.

[27] Cai B, Adams BL, Nelson TW. Relation between precipitate-free zone width and grain boundary type in 7075-T7 Al alloy [Journal Article]. Acta Materialia. 2007;55(5):1543–1553. Available from: `http://www.sciencedirect.com/science/article/pii/S1359645406007403`.
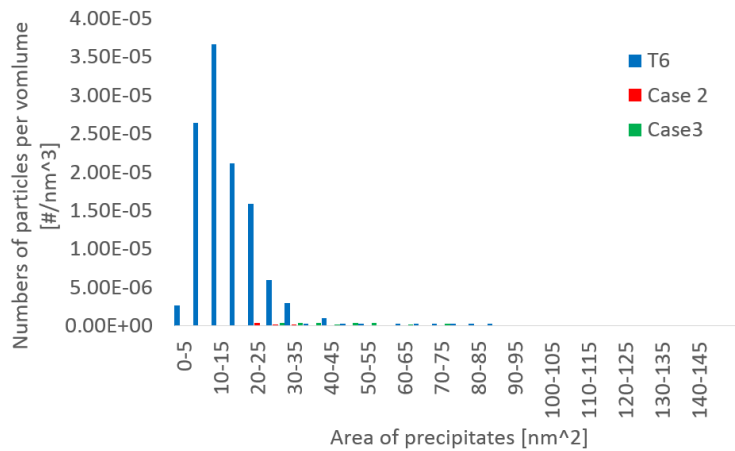
Appendix

Below are the distributions for area and length for all three cases, distributed as particles per volume.
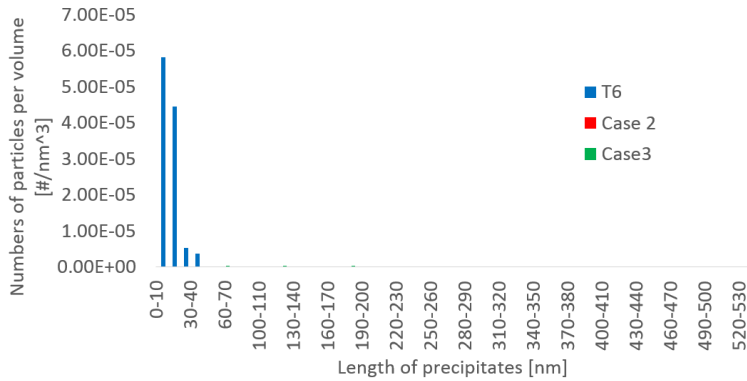
Figure 7.1: Length distribution for all cases. Particles per volume.

Figure 7.2: Length distribution for all cases. Particles per volume.